HHS Public Access

Author manuscript

Nat Cell Biol. Author manuscript; available in PMC 2024 November 07.

Published in final edited form as:

Nat Cell Biol. 2024 September ; 26(9): 1482–1495. doi:10.1038/s41556-024-01480-1.

TorsinA is essential for neuronal nuclear pore complex localization and maturation

Sumin Kim[1,2,^], **Sébastien Phan**[3], **Hung Tri Tran**[4,5], **Thomas R. Shaw**[6,7], **Sarah H. Shahmoradian**[4,5,8], **Mark H. Ellisman**[3], **Sarah L. Veatch**[6,7], **Sami J. Barmada**[1,2,*], **Samuel S. Pappas**[4,9,*], **William T. Dauer**[4,9,10,*]

[1]Cellular and Molecular Biology Graduate Program, University of Michigan, Ann Arbor, MI;

[2]Department of Neurology, University of Michigan, Ann Arbor, MI;

[3]National Center for Microscopy and Imaging Research, Center for Research on Biological Systems, Department of Neurosciences, School of Medicine, University of California San Diego, La Jolla, CA;

[4]Peter O'Donnell Jr. Brain Institute, UT Southwestern, Dallas, TX;

[5]Center for Alzheimer's and Neurodegenerative Diseases, UT Southwestern, Dallas, TX;

[6]Department of Biophysics, University of Michigan, Ann Arbor, MI;

[7]Program in Applied Biophysics, University of Michigan, Ann Arbor, MI;

[8]Department of Biophysics, UT Southwestern, Dallas, TX;

[9]Department of Neurology, UT Southwestern, Dallas, TX;

[10]Department of Neuroscience, UT Southwestern, Dallas, TX;

Abstract

As lifelong interphase cells, neurons face an array of unique challenges. A key challenge is regulating nuclear pore complex (NPC) biogenesis and localization, the mechanisms of which are largely unknown. Here, we identify neuronal maturation as a period of strongly upregulated NPC biogenesis. We demonstrate that the AAA+ protein torsinA, whose dysfunction causes the neurodevelopmental movement disorder DYT-*TOR1A* (DYT1) dystonia, coordinates NPC spatial organization without impacting total NPC density. We generated an endogenous Nup107-HaloTag mouse line to directly visualize NPC organization in developing neurons and find that torsinA is

[*]Co-corresponding authors; William T. Dauer: William.Dauer@utsouthwestern.edu; Samuel S. Pappas: Samuel.Pappas@utsouthwestern.edu; Sami J. Barmada: sbarmada@med.umich.edu.

[^]Current address: Department of Biological Engineering, Massachusetts Institute of Technology, Cambridge, MA;

Author contributions:

S.K., S.S.P., S.J.B., and W.T.D. conceived the study. S.K., H.T.T., and S.S.P. performed experiments. STEM tomograms were acquired by S.P. in M.H.E's laboratory. S.K., S.L.V., T.R.S., and S.P. analyzed data. S.K. and S.S.P. wrote the manuscript. S.K. prepared the figures. S.L.V., S.J.B., S.H.S, and W.T.D. contributed to revisions. All authors reviewed the manuscript.

Competing interests:

None.

Code availability

FIJI, MATLAB, and python scripts for SIM and confocal analyses are available on https://github.com/suminkim/NPC_NE_measurements. Scripts for dSTORM analyses are available on https://github.com/VeatchLab/smlm-analysis.

essential for proper NPC localization. In the absence of torsinA, the inner nuclear membrane buds excessively at sites of mislocalized nascent NPCs, and formation of complete NPCs is delayed. Our work demonstrates that NPC spatial organization and number are independently determined and identifies NPC biogenesis as a process vulnerable to neurodevelopmental disease insults.

Nuclear pore complexes (NPCs) are large multiprotein assemblies that allow passive diffusion of small molecules and facilitate nucleocytosolic transport of proteins and RNA[1,2]. Regulation of NPCs is important in neurons[3,4], as neuronal plasticity depends on nuclear transport of signaling molecules[5–8] and neurodevelopmental processes rely on local translation of exported mRNAs[9–13]. NPC abnormalities occur in several nervous system diseases[14–18] and mutations in nucleoporins cause early-onset neurological illness[19,20]. Unlike mitotic cells, neurons manage NPC number and localization within a closed interphase nucleus. Neuronal NPCs exhibit minimal turnover and nucleoporins (Nups) that constitute the NPC are among the longest-lived proteins[21,22], underscoring the unique challenge neurons face in regulating NPC formation and function. Despite the biological and clinical importance of these events, little is understood about neuronal NPC biogenesis or the mechanisms regulating NPC number and spatial organization.

TorsinA, a AAA+ protein in the endoplasmic reticulum (ER)/nuclear envelope (NE) lumen[23–31], lies at the intersection of neuronal NPC biogenesis and neurodevelopmental disease. The neurodevelopmental movement disorder DYT-*TOR1A* (DYT1) dystonia is caused by an in-frame 3-bp deletion in the *TOR1A* gene that encodes a ΔE-torsinA mutant protein[32,33]. The NE is an active site of torsinA activity[26,27,34,35] and nuclear membrane proteins are mislocalized in *C. elegans* germ cells lacking the torsin homolog OOC-5[36].

TorsinA-knockout (KO) or homozygous ΔE mutant mice develop abnormal NE evaginations (“blebs”) exclusively in post-migratory maturing neurons[37]. Consistent with biochemical studies[38,39], these observations establish ΔE as a loss-of-function (LOF) mutation. NE blebs are inner nuclear membrane (INM) outpouchings that emerge during early postnatal maturation and subsequently resolve without causing cell death[37,40,41]. Non-neural tissue and mitotic cell lines lacking torsinA do not exhibit NE abnormalities[42–44], highlighting a unique role for torsinA in neurons. Clinical manifestation of DYT1[45] and *in vivo* studies demonstrate that torsinA function is essential selectively during early postnatal neural development[46].

The INM budding characteristic of NE blebs suggests a link to interphase NPC assembly, in which NPCs are inserted *de novo* into an intact nuclear membrane via INM budding and subsequent fusion with the outer nuclear membrane (ONM)[47–49]. Dissimilar to the budding that occurs in normal NPC assembly, NE blebs enlarge and do not fuse with the ONM. Maturing torsinA-KO neurons also develop mislocalized clusters of nucleoporins in the nuclear envelope. Strikingly, NE blebs are present only transiently during early postnatal development, whereas abnormal NPC clusters persist into adulthood in DYT1 mouse models[15,46]. These clusters contain Nup153, an early-recruited NPC component, but lack the cytoplasmic nucleoporin Nup358 (recruited after INM-ONM fusion[47]). The lack of INM-ONM fusion in NE blebs and the absence of Nup358 in nucleoporin clusters suggests that these two phenotypes may be related, implicating torsinA function in NPC biogenesis.

Mitotic cells lacking multiple torsin paralogs develop NE blebs that co-localize with NPC components and are downregulated by blocking interphase NPC assembly[42,50]. NE blebs are not observed with a single torsinA deletion and nucleoporin distribution appears normal in these cells[44,50], limiting the use of mitotic cells for exploring torsinA biology in a disease-relevant context. Little is known about these clusters, including their relationship to NE blebs, whether they contain formed (but mislocalized) NPCs or aggregated nucleoporins, and how they relate to NPC assembly.

Here, we identify a unique role for torsinA in the localization and maturation of nascent neuronal NPCs. We find that NPC formation is strongly upregulated during a distinct neurodevelopmental window. To study physiological NPC biogenesis in neurons, we created knock-in mice harboring HaloTag-Nup107 allele. Pulse-chase studies in primary neurons derived from these mice demonstrate that torsinA is essential for the normal localization of nascent NPCs. Abnormal clusters containing mislocalized NPCs arise simultaneously with the emergence of NE blebs in torsinA-KO neurons. Ultrastructural evidence demonstrates that NE blebs form at the sites of NPC biogenesis and represent a stalled intermediate step of NPC assembly. While abnormal NPC clusters persist, NE blebs resolve in mature neurons. Completion of new NPCs is delayed, but not permanently halted, in torsinA-KO neurons, indicating that INM-ONM fusion can proceed in the absence of torsinA. Our work advances understanding of NPC spatial organization by identifying a determinant of NPC localization and highlights a critical role for torsinA in NPC biogenesis during a discrete developmental window.

Results

NPC biogenesis is upregulated during neuronal maturation

To explore neuronal NPC biogenesis, we used structured illumination microscopy (SIM) to characterize NPC density in cortical primary neurons. Primary neurons from wildtype P0 (postnatal day 0) pups were cultured and fixed between days in vitro (DIV) 4 and 24, during which they develop and reach maturity[51]. Neurons were labeled with Nup153, Nup98, and Map2 antibodies and SIM imaging of Nup153 and Nup98 was carried out on neurons expressing the neuronal marker Map2. In immature neurons[51] (i.e., DIV4 and DIV6), both nucleoporins (Nups) appeared sparse. As the neurons matured, the density of Nup153 and Nup98 puncta increased, culminating in a dense yet even distribution of NPCs across the nuclear envelope (DIV18 and DIV24; Fig. 1a, Extended Data Fig. 1a). We developed an image analysis pipeline to quantitatively measure Nup density and distances (Extended Data Fig. 1b). Peaks from Nup153 and 98 puncta mostly overlapped, suggesting that this staining labeled NPCs rather than non-NPC pools of nucleoporins. The density of Nup153 and Nup98 puncta gradually increased from approximately 7 puncta/μm^2 at DIV4 to 14 puncta/μm^2 at DIV24 (Fig. 1b, c). Nuclear area did not change significantly (Extended Data Fig. 1c), indicating that the increased Nup density is due to *de novo* formation of new NPCs. We next calculated the nearest neighbor distance for each punctum (Extended Data Fig. 1d, e). As expected, few puncta at any timepoint measured had a nearest neighbor within 120nm, the diameter of a single NPC[52,53]. The percentage of Nup153 and Nup98 puncta with a nearest neighbor within a two-pore diameter distance (240nm) increased with time,

while the percentage of puncta with a nearest neighbor far away decreased. Consistent with increasing NPC density, the proportion of Nup puncta with multiple proximal neighbors increased as neurons matured (Fig. 1d, e). These data demonstrate that NPC biogenesis is upregulated during neuronal maturation.

To further explore NPC biogenesis, we measured nuclear rim intensity of multiple Nups in Map2-positive neurons with confocal microscopy. There was an approximately twofold increase in nuclear rim intensity of Nup153 and Nup98 between DIV4 and DIV10 (Extended Data Fig. 2a–c), as well as Nups containing Phe-Gly motifs (mab414) and Nup210 (a transmembrane nucleoporin) (Extended Data Fig. 2d–f). These data indicate upregulated density of multiple NPC components, including those spanning the nuclear basket, inner ring, and transmembrane subunits.

TorsinA is essential for NPC localization but not density

We reported previously that torsinA deletion causes long-lasting abnormal nucleoporin clusters in neurons[15]. To determine if cluster formation coincides with NPC biogenesis, we fixed maturing wildtype (WT) and torsinA-KO neurons at DIV4, 6, 8, 10, and 14 and labeled NPCs using anti-Nup153 and anti-Nup98 antibodies. At DIV4, Nup153 and Nup98 were sparsely localized in both WT and torsinA-KO neurons with indistinguishable distribution between genotypes (Fig. 2a, b). While nucleoporin organization remained uniform in maturing WT neurons, DIV6 torsinA-KO neurons exhibited small clusters that multiplied and enlarged over time (Fig. 2a, b). Mature torsinA-KO neurons displayed strikingly large clusters, contrary to the dense but uniform distribution observed in mature WT neurons. We conducted an autocorrelation analysis to quantitatively characterize changes in nucleoporin spatial correlation across developmental age (Extended Data Fig. 3a, b). The density of particles is roughly inversely correlates to the amplitude of the autocorrelation curve, and autocorrelation values indicate dispersion (<1) or clustering (>1). The decreasing amplitude of the autocorrelation curve reflected increasing density over time for both WT and torsinA-KO neurons. Broadening of the curve for torsinA-KO neurons indicated growing clusters (Extended Data Fig. 3a). We normalized autocorrelation to total density at each timepoint to account for amplitude dependence on density. In WT neurons, normalized autocorrelation curves at all timepoints exhibited a dip <1 around 200nm indicating dispersion of nucleoporins at this distance (Extended Data Fig. 3b). In contrast, the normalized autocorrelation increased over time for torsinA-KO neurons, reflecting progressively worsening clusters.

To determine whether abnormal nucleoporin clusters contain structures resembling normal NPCs, we conducted direct stochastic optical reconstruction microscopy (dSTORM) of Nup210-labeled DIV10 neurons. WT neurons showed clear, uniformly distributed NPC structures containing central channels (Fig. 2c). Similar NPC structures containing central channels were observed in torsinA-KO DIV10 neurons within clusters. In WT neurons, autocorrelation was <1 between 150nm and 400nm, indicating dispersion, while autocorrelation >1 was observed in torsinA-KO neurons, reflecting clustering (Extended Data Fig. 3c). To further analyze spatial organization and structure of individual NPCs, we segmented individual NPCs. Plotting the nearest neighbor distance between centroids

of segmented NPCs in WT neurons yielded two distinct peaks, indicating regular spatial organization of NPCs (Extended Data Fig. 3d). In torsinA-KO neurons, the second peak was absent, reflecting abnormal NPC spacing. To assess NPC size, we aligned and averaged segmented NPCs (Fig. 2d) and calculated their radii (Fig. 2e). The average WT NPC exhibited a radius of 39nm +/− 0.3nm, while the average KO NPC had a smaller radius of 37.3 +/− 0.2nm. These data indicate that abnormal nucleoporin clusters in torsinA-KO neurons represent aberrantly localized clusters of NPCs rather than unstructured aggregates. Herein we refer to nucleoporin clusters as NPC clusters.

We calculated NPC density in WT and torsinA-KO neurons from SIM images (Fig. 2a, b), incorporating Nup puncta in clusters. Despite striking spatial differences, there was no significant difference in average NPC density between WT and torsinA-KO neurons at any age (Fig. 2f, g, Extended Data Fig. 3e, f), indicating that maturing WT and torsinA-KO neurons similarly upregulate NPC biogenesis. Nuclear area and shape did not differ significantly between WT and torsinA-KO neurons and abnormal NPC clusters did not correspond to local folds or dips in the lamin meshwork (Extended Data Fig. 3g–i). These data strongly suggest that torsinA is essential for the proper spatial organization, but not total density, of NPCs.

HaloTag-Nup107 knock-in enables endogenous NPC labeling

To dissect mechanistically how NPC clusters form, we developed a knock-in mouse line in which HaloTag[54] is fused to Nup107 to track endogenous NPC biogenesis (Extended Data Fig. 4a). Nup107 was chosen as 3x-EGFP-Nup107 maintains normal localization and dynamics[55,56]. We validated this HaloTag-Nup107 (Halo-Nup107) knock-in mouse line using JF646 HaloTag ligand to label endogenous Nup107 protein in DIV10 primary neurons (Fig. 3a). We observed a gene dose-dependent increase in fluorescence intensity at the nuclear membrane in neurons derived from $Nup107^{+/+}$, $Nup107^{KI/+}$, $Nup107^{KI/KI}$ mice, indicating that the fusion protein is incorporated into NPCs. Probing the levels of the Nup107-HaloTag fusion protein in P0 cortical lysates further validated the knock-in (Extended Data Fig. 4b). $Nup107^{KI/KI}$ mice were indistinguishable from their WT littermate controls and we observed the expected Mendelian ratios of genotypes from a $Nup107^{KI/+}$ intercross (Extended Data Fig. 4c), indicating that the HaloTag did not exert toxicity.

We examined the localization and density of HaloTag-Nup107 in developing neurons by labeling DIV4, 10, and 18 $Nup107^{KI/KI}$ neurons with the JFX554 HaloTag ligand and staining them with Nup153 antibody. SIM imaging demonstrated an approximately twofold increase in Nup density from DIV4 to DIV18 despite similar nuclear envelope area (Fig. 3b–d, Extended Data Fig. 4d). Nup153 and JFX554 showed a high level of colocalization (Extended Data Fig. 4e, f). Nearest neighbor distances of HaloTag-Nup107 puncta decreased throughout neuronal maturation while the number of neighboring puncta within 240nm increased, reflecting increased density and decreased pore-pore distances as neurons mature (Extended Data Fig. 4g, h). To determine if NPC density increases *in vivo*, we labeled brain slices from P0 and P14 $Nup107^{KI/KI}$ mice with the JFX650 HaloTag ligand, revealing an approximately 2.5-fold increase in NPC density between P0 and P14 (Fig. 3e, f). Remarkably, this density increase occurs concurrently with growing nuclear size (~2 fold

increase in nuclear area; Fig 3g), suggesting that total neuronal NPC number increases ~5-fold in the first two weeks of postnatal development, consistent with a previous report using electron microscopy[57]. These data validate the HaloTag-Nup107 mouse model as a tool for studying endogenous NPC dynamics and confirm that maturing neurons exhibit strongly upregulated NPC biogenesis *in vitro* and *in vivo*.

To examine endogenous Nup107 in torsinA mutant neurons, we intercrossed *Nup107*$^{KI/KI}$ mice with *Tor1a*$^{+/-}$ and *Tor1a*$^{+/\Delta E}$ mouse lines[37] (Extended Data Fig. 4i). We probed for HaloTag-Nup107 in WT (*Tor1a*$^{+/+}$;*Nup107*$^{KI/KI}$) or torsinA-KO (*Tor1a*$^{-/-}$;*Nup107*$^{KI/KI}$) DIV10 neurons and observed abnormal NPC clusters in torsinA-KO neurons as expected (Figure 3h, h'). Abnormal clusters were also observed in DIV10 neurons harboring the disease-relevant ΔE allele (torsinA-ΔE/ΔE; Figure 3i, i'), further demonstrating a link between NPC clustering and DYT1 pathophysiology. WT, torsinA-KO, and torsinA-ΔE/ΔE exhibited similar Nup153 nuclear rim intensity (Fig. 3j, k), indicating that the ΔE mutation, similar to torsinA-KO, impacts NPC localization without affecting total NPC density.

Sites of NPC biogenesis are abnormal in torsinA-KO neurons

NPC clusters can form via two possible mechanisms: (i) rearrangement of NPCs post-formation, and (ii) improper localization of *de novo* assembling NPCs. If NPCs rearrange into clusters post-formation in torsinA-KO neurons, clustering of both pulse- and chase-labeled NPCs is expected (Fig. 4a, top). In contrast, if sites of new NPC biogenesis are mislocalized in the absence of torsinA, clustering of exclusively chase-labeled NPCs would be observed (Fig. 4a, bottom).

To test these mechanisms, we performed a pulse-chase experiment using HaloTag-Nup107 neurons to label NPCs formed at different stages of neuronal maturation. Neurons from WT (*Tor1a*$^{+/+}$;*Nup107*$^{KI/KI}$) or torsinA-KO (*Tor1a*$^{-/-}$;*Nup107*$^{KI/KI}$) mice were labeled with JFX554 HaloTag ligand from DIV3 to DIV4 to saturate labeling of all existing Nup107. Following dye washout, JF646-containing media was used to label NPCs formed between DIV4 and time of fixation (Fig. 4b). This pulse-chase labeling approach allowed us to distinguish NPCs formed up to DIV4 from those formed at DIV4-6, DIV4-8, or DIV4-10. Consistent with our previous findings, NPC biogenesis was upregulated in both genotypes and torsinA-KO neurons exhibited clustered NPCs (Fig. 4c, Extended Data Fig. 5a). The density of pulse-labeled (JFX554) NPCs remained constant over time (Fig. 4d, Extended Data Fig. 5b) while the density of newly formed NPCs (new JF646; JF646-positive NPCs not overlapping with JFX554) increased in both WT and torsinA-KO neurons (Fig. 4d, Extended Data Fig. 5c), indicating successful pulse-chase labeling. JFX554-labeled NPCs maintained sparse distribution at all timepoints in both genotypes, even in DIV10 torsinA-KO neurons that contained large NPC clusters as observed via Nup153 labeling (Fig. 4e, Extended Data Fig. 5d). In WT neurons, NPCs assembling after DIV4 localized in empty spaces devoid of existing NPCs, preserving an overall uniform pattern of NPC distribution. In contrast, new NPCs assembling after DIV4 in torsinA-KO neurons abnormally formed in close proximity, creating increasingly large clusters (Fig. 4f, Extended Data Fig. 5e). These data support a mechanism in which mislocalization of newly forming NPCs leads to NPC clusters in torsinA-KO neurons. These data suggest that torsinA is an essential factor in

determining sites of *de novo* NPC biogenesis and demonstrate that in developing neurons, the spatial organization of NPCs is determined by the site of NPC formation rather than by post-formation rearrangement.

NE blebs form at sites of NPC biogenesis

Abnormal NE blebs form selectively in post-migratory neurons in the torsinA-KO nervous system[37,41]. To probe the potential link between NE bleb formation and NPC biogenesis, we examined the NE of WT and torsinA-KO neurons at DIV4 and DIV10, as NPC density increases and abnormal clusters emerge during this period. Using transmission electron microscopy, we observed NE blebs in torsinA-KO neurons at both DIV4 and DIV10 (Fig. 5a). Significantly more cells exhibited NE blebs at DIV10 (Fig. 5b) and bleb frequency increased dramatically from DIV4 to DIV10 (Fig. 5c), demonstrating a temporal link between NE bleb formation and NPC biogenesis.

We next explored whether NE blebs and NPC clusters overlap spatially. We generated 3D volumes of WT and torsinA-KO DIV10 neuronal nuclear envelopes using intermediate high voltage scanning transmission electron microscopy (STEM) and multi-tilt electron tomography (Supplementary Video 1). We observed NE blebs both as isolated entities and in clusters of several blebs enclosed within a single stretch of the ONM (Supplementary Video 1, Extended Data Fig. 6a). Every bleb connected to the NE via a pore channel that appeared similar to wildtype NPC channels (Fig. 5d–f, Supplementary Video 2), resulting in corresponding clusters of pores (Extended Data Fig. 6a, b). In contrast, non-bleb-associated “regular” NPCs were dispersed throughout the NE (Extended Data Fig. 6a, b, Supplementary Video 1) and did not form clusters in any tomogram. We annotated every pore from all tomograms and categorized them based on their association with blebs. Projection of all annotated torsinA-KO pores (both regular and bleb-associated) showed clustered distribution similar to SIM images of mature torsinA-KO neurons (Extended Data Fig. 6b). We did not observe vesicles reminiscent of large ribonucleoprotein granules reported in torsin mutant *Drosophila* cells[58]. These data suggest that the mislocalized NPC clusters observed with light microscopy are associated with NE blebs. To confirm the spatial link between NPC clusters and NE blebs, we co-labeled NPCs and blebs by staining DIV10 neurons for Nup153 and Ubiquitin-K48, which is enriched in NE blebs[40,42,50,59]. Line scan analyses showed Ubiquitin-K48 accumulation adjacent to Nup153 clusters in torsinA-KO neurons (Extended Data Fig. 7). The temporal and spatial connection between NE bleb and NPC formation support the hypothesis that NE blebs form at the sites of nascent NPCs in torsinA-KO neurons.

The 3D volumes also allowed us to analyze the dimensions of pore channels from WT and torsinA-KO neurons (Extended Data Fig. 6c). On average, the diameter of a pore in WT neurons was 80nm. Regular (non-bleb-associated) pores in torsinA-KO neurons were slightly narrower, at 74.6nm, and bleb-associated KO pores were even smaller (69.8nm). These data are consistent with our dSTORM data and demonstrate that even regular NPCs with fully-formed pore channels in torsinA-KO neurons may not be able to dilate to the same degree as WT NPCs. We also found that the central plugs of bleb-associated pores facing the nucleoplasm are more electron dense compared to the plugs of regular pores, even

within the same torsinA-KO neuron (Extended Data Fig. 6d, e). While the identity of these central plugs is unclear, they appear similar to plugs observed in immature NPCs[47,60].

Completion of NPC assembly is delayed in torsinA-KO neurons

NE blebs are transient in vivo, resolving without causing cell death[40,41]. We examined the NE in DIV10 and DIV18 WT and torsinA-KO neurons because synaptogenesis peaks and remains stable after the first two weeks in culture[51] and our SIM data suggests that NPC density may begin to plateau by DIV18. Both the prevalence and frequency of NE blebs decreased significantly between DIV10 and DIV18 in torsinA-KO neurons (Fig. 6a–c). Regions of the NE contained multiple adjacent complete NPCs marked by fused INM and ONM in DIV18 torsinA-KO neurons (Fig. 6a, last panel). We hypothesized that NPC assembly completes upon the resolution of NE blebs and assessed NPC assembly states by labeling early- (Nup153) and late-recruited (Nup358) components at DIV10 and DIV18. At DIV10, Nup153 nuclear rim intensity was similar between torsinA-KO and WT neurons, but Nup358 localization was reduced in torsinA-KO neurons (Fig. 6d–g). These data are consistent with our previous report[15] and indicate that NPCs are stalled at an intermediate state in the absence of torsinA at this timepoint. At DIV18, Nup358 was present in Nup153-positive NPC clusters and fluorescence intensity was restored (Fig. 6g). Single-NPC resolution using SIM (Extended Data Fig. 8a) confirmed that Nup358 was sparsely distributed and failed to localize to clusters containing Nup153 in DIV10 torsinA-KO neurons. At DIV18, Nup358 exhibited clustered localization that overlapped with Nup153-positive clusters. In contrast, most NPCs were labeled with both Nup153 and Nup358 in WT DIV10 neurons. Notably, NPCs remained clustered in DIV18 torsinA-KO neurons (Extended Data Fig. 8b, c). At DIV18, the average torsinA-KO NPC channel remains smaller than that of the average WT NPC (Extended. Data Fig. 8d), suggesting that even complete NPCs in torsinA-KO neurons may be structurally distinct from those in WT neurons.

Nup358 recruitment to halted bleb-associated NPC assembly intermediates could occur by either (i) resumed assembly upon bleb resolution, or (ii) remodeling through degradation. To assess whether bleb-associated NPCs undergo remodeling, we conducted a pulse-chase study of WT (*Tor1a*$^{+/+}$;*Nup107*$^{KI/KI}$) and torsinA-KO (*Tor1a*$^{-/-}$;*Nup107*$^{KI/KI}$) neurons from DIV10 to DIV18, during which blebs resolve. We labeled all existing Nup107 at DIV10 with JFX554 HaloTag ligand (pulse) and labeled new Nup107 with JF646 HaloTag ligand (chase) from DIV10 to DIV18. JFX554 signal decreased between DIV10 and 18 in both WT and torsinA-KO neurons while JF646 labeling appeared (Extended Data Fig. 8e). Nup358 intensity increased in both WT and torsinA-KO neurons as expected (Extended Data Fig. 8f) while JFX554 intensity decreased to less than 50% of the original DIV10 fluorescence (Extended Data Fig. 8g). These data indicate that Nup107 undergoes turnover between DIV10 and 18. Although we cannot distinguish whether Nup107 proteins are replaced within existing NPCs or NPC intermediates are completely turned over, this remodeling occurs in both WT and torsinA-KO neurons and is not specific to blebs. These data indicate that torsinA may not directly mediate fusion of the inner and outer nuclear membranes during interphase NPC assembly in neurons, as loss of torsinA causes delayed, rather than permanently halted, NPC biogenesis.

Discussion

Our work establishes torsinA as essential for the normal localization and assembly kinetics of interphase NPC biogenesis in neurons (Extended Data Fig. 9a, b). We identify postnatal neuronal maturation as a previously unappreciated context of strongly and steadily upregulated NPC biogenesis. NPC biogenesis initiates at abnormal sites in torsinA-KO neurons, resulting in tightly packed NPC clusters that contain central pore channels. Onset of NPC formation and NPC density remain normal, suggesting that NPC number and localization are governed by distinct mechanisms. Mislocalized NPC biogenesis represents the earliest known torsinA loss-of-function phenotype, indicating that subsequent phenotypes may be downstream of torsinA function. Unlike the persistent NPC clusters, NE blebs resolve over time and formation of mature, completed NPCs is delayed, but not permanently halted. Our experiments define a molecular determinant of the poorly understood process of NPC spatial organization and identify neuronal maturation-triggered NPC biogenesis as a unique torsinA-dependent process during a neurodevelopmental critical period.

Post-migratory maturing neurons must meet the large demand for protein synthesis to integrate into synaptically-connected circuits[51]. Considerable work in non-neuronal cells indicates that increasing NPC number is needed to support such metabolic demand[60–62], but similar studies of NPC biogenesis have not been performed in neurons. We demonstrate a doubling of neuronal NPC density from DIV4 to DIV18 and an even greater degree of NPC density increase in cortical brain tissue between P0 and P14 that occurs even as nuclear size grows, consistent with the *in vivo* increase observed in a previous EM study[57]. The robust upregulation of neuronal NPC density contrasts with interphase NPC assembly in mitotic cells, which occurs concomitantly with NE expansion with little to no increase in NPC density[56,63–66]. While neuronal NPC biogenesis is sustained over two weeks, interphase NPC assembly in mitotic cells completes within hours[47,56,63–65,67]. Protein levels are upregulated during the first twenty days of maturing primary cortical neurons, coinciding with synaptogenesis and increasing morphological complexity[51]. The prolonged neuronal NPC biogenesis may accommodate an increased need for nucleocytoplasmic transport during neural development. Although NPC assembly in neurons and interphasic mitotic cells both involve a *de novo* insertion of NPCs in intact nuclear membranes[47–49,64,65,68], these differences in assembly timescale and the unique process of neuronal maturation suggest possible neuron-specific regulators of NPC biogenesis. Our NPC distribution analyses demonstrate that WT NPCs are evenly dispersed at all timepoints assessed, as observed in other cell types[69], suggesting an unknown mechanism maintains NPC spacing.

The DIV4–10 pulse-chase study of endogenous HaloTag-Nup107 demonstrates that torsinA loss causes NPCs to form abnormally close to one another, implicating that torsinA determines nascent NPC localization in neurons. Although post-formation NPC rearrangement is observed in yeast[70,71], we find no evidence to support this alternative mechanism for clustering in neurons; NPCs formed in immature torsinA-KO neurons remain normally distributed throughout neuronal maturation. These normally distributed NPCs may be formed via a postmitotic NPC assembly mechanism prior to terminal neuronal differentiation, since torsinA loss does not cause NPC abnormalities in mitotic cells[42,44].

Our pulse-chase and *in vivo* studies in HaloTag-Nup107 knock-in mice highlight the utility of this new reagent for the study of NPC biology in diverse tissues and contexts, including in disease models. Beyond the studies we performed, HaloTag-Nup107 could be used for cell sorting, biochemical assays, or live-cell imaging of NPC dynamics.

It is unclear how torsinA ensures localization of nascent NPCs. NPC formation may require a specific lipid microenvironment that is maintained by torsinA. Lipid sensing and metabolism are active at the INM[72–77] and lipids contribute to NPC assembly[78]. The *Drosophila* torsin ortholog dTor maintains lipid homeostasis at the nuclear membrane[44,79,80], and torsinA plays a role in mammalian hepatic lipid metabolism[81]. While no difference in lipids were found in mitotic cells lacking torsins[42], NPC clustering is not observed in these nonneuronal cells. Future studies may reveal neural-specific spatial anomalies of specific lipids or lipid-binding proteins related to aberrant NPC localization.

The channel widths of bleb-associated pores in DIV10 torsinA-KO neurons are smaller than that of regular NPCs. Interphase NPC assembly involves lateral dilation of the budding NPC prior to INM and ONM fusion[47–49], suggesting that the smaller central channel could reflect stalled assembly intermediates that have not yet fully dilated. Consistent with this possibility, NE blebs emerge concurrently with upregulated NPC biogenesis and spatially correlate with mislocalized NPCs. These findings are similar to previous reports of NE blebs colocalizing with NPC components in mitotic cells lacking multiple torsin paralogs[42]. We observe electron dense central plugs on the nucleoplasmic side of NE bleb-associated pores, which appear similar to plugs reported in newly forming NPCs[47,60] and may represent unique machinery present in intermediate NPC structures.

Prior observations suggested that torsinA may be involved in the INM-ONM fusion step of interphase NPC assembly. Nup358 is not recruited to Nup153-positive clusters in DIV10 torsinA-KO neurons[15] or interphase-formed NPCs in torsin-deficient mitotic cells[50]. Data from mitotic cells lacking torsins also led to the hypothesis that NE blebs are a consequence of defective NPC assembly[50,82–84]. We demonstrate that INM-ONM fusion can occur in the absence of torsinA and that formation of fully assembled NPCs is delayed, but not halted. While DIV10 torsinA-KO neurons exhibit numerous NE blebs, these blebs resolve as neurons mature, as observed *in vivo*[41]. NE bleb resolution accompanies NPC assembly completion, as Nup358 is present in Nup153-positive NPC clusters in DIV18 torsinA-KO neurons. This contrasts with findings in mitotic cells lacking multiple torsin paralogs[42,50,82], in which completion of NPC assembly is not observed, possibly due to the difference in timescale of assembly between the cell types or lack of torsin paralogs. Based on our observations, we propose that NE blebs pose a physical barrier to the continuation of NPC assembly. The disrupted sites of NPC biogenesis precede formation of NE blebs which are likely indirect downstream events with unclear origins. Excessive INM budding during NPC biogenesis may be due to lipid imbalance, and NPC assembly abnormalities could be secondary to torsinA-related lipid defects[44,79,80]. We do not exclude the possibility of torsins' involvement in INM-ONM fusion. The timing of NE bleb resolution correlates with the dynamics of the torsinA paralog torsinB, which increases expression as NE blebs resolve[41]. Ablating torsinB prevents NE bleb resolution in torsinA-KO neurons and induces NE blebs in torsinA-deficient non-neuronal cells[41], whereas overexpression

of torsinB rescues torsinA-related motor deficits and neuropathology caused by torsinA loss-of-function[85].

NPC abnormalities may contribute to neural dysfunction. NPCs in torsinA-KO neurons are smaller than WT NPCs, raising the possibility that a narrow channel could limit the size of molecules that can diffuse through the NPCs. Protein nucleocytoplasmic transport is compromised in maturing torsinA-KO neurons[15], which may negatively impact nucleocytoplasmic transport-dependent neural functions such as synaptic plasticity[5–8], dysfunction of which is linked to the clinical manifestation of dystonia[86,87]. Delayed NPC assembly may interfere with transport of locally translated RNA critical for neurodevelopmental processes such as dendritic outgrowth, axonal guidance and synaptogenesis[9–13], which is altered in torsinA-KO[88] and torsinA-ΔE knock-in brains[89–92]. Nucleoporins physically interact with the genome and influence transcription, and changing their expression results in differential NPC assemblies and alters neural differentiation[93–102]. NPC mislocalization may therefore lead to transcriptomic changes by altering the chromatin landscape and lead to functional abnormalities in maturing postnatal neurons.

Aberrant NPC clustering is present in adult torsinA-mutant mice after NE bleb resolution and NPC assembly completion[15,46], likely reflecting the long-lived nature of neuronal NPCs. NPC density remains unchanged between 6 weeks and 2 years of age in rat brains[22] and between postnatal days 15 and 180 in the mouse cortex[57], and NPC components turn over at different rates[22]. Once formed, NPCs are unlikely to turnover as a whole complex. Our previously published *in vivo* data demonstrates a unique critical period for torsinA function in the nervous system during neural maturation[46,103]. Embryonic, but not adult, deletion of torsinA causes NPC clustering to emerge during postnatal maturation[46,59]. Our findings establish NPC biogenesis as a key molecular event of this neurodevelopmental critical period and raise the possibility that NPC-related processes may underlie additional critical periods in normal development as well as early- and late-onset neurological disorders.

Methods:

Mice

All animal work described in this manuscript has been approved and conducted under the oversight of the UT Southwestern and the University of Michigan Institutional Animal Care and Use Committees. Experimental procedures were conducted in accordance with the approved protocols and the National Institutes of Health Guide for the care and use of laboratory animals. Mice were maintained in a temperature-, humidity-, and light-controlled (12h light, 12h dark) animal facility room with access to food and water *ad libitum*. All mice are of C57BL/6j; 129 background. *Tor1a*$^{-/-}$ and *Tor1a*$^{+/+}$ mice were derived from *Tor1a*$^{+/-}$ intercross[37]. Mice of both sex were used for this study.

Generation of HaloTag-Nup107 mouse line

The HaloTag-Nup107 mouse line was generated using CRISPR/Extreme Genome Editing technology in partnership with Biocytogen. HaloTag with a short linker and TEV

site was inserted immediately upstream of the Nup107 start codon. *Nup107*$^{KI/KI}$ mice were crossed into *Tor1a*$^{+/-}$ line[37] to generate *Nup107*$^{KI/KI}$ *Tor1a*$^{+/-}$ breeders. The following primers were used for genotyping: TGTGCTTCCGGAGAGCGGGAAG, ATAGGTTTGCCTGAAACTCCTGTGAC, and CGTGGTCGTCGAAGAAATAACCCAG. PCR cycle (95°C, 3 min; 95°C, 15 s; 70°C, 20 s (−0.7°C/c); 72°C, 1 min, 15 cycles; 98°C, 15 s; 60°C, 20 s; 72°C, 1 min, 25 cycles; 72°C, 7 min) yielded bands at 681bp for WT and 341bp for Nup107 knock-in.

Primary neuron culturing

Brains were isolated from P0 pups into ice cold, filtered dissection buffer (6.85 mM sodium chloride, 0.27mM potassium chloride, 0.0085mM sodium phosphate dibasic anhydrous, 0.011mM potassium phosphate monobasic anhydrous, 33.3mM D-glucose, 43.8mM sucrose, 0.277mM HEPES, pH 7.4). After removing the cerebellum and the meninges, cortices were dissected out, placed into a microcentrifuge tube, cut into small pieces with dissection forceps, and incubated in 50μL papain (2mg/mL; BrainBits) and 10μL DNase I (1mg/mL; Worthington Biochemical) for 30min at 37 °C. 500μL BrainPhys Neuronal Medium (Stemcell Technologies) and 10μL additional DNase I were added, and cortices were triturated using P1000 and P200 pipet tips, then centrifuged at 125x*g* for 5min. Supernatant was discarded and pellets were triturated and centrifuged three more times. Pelleted neurons were resuspended in BrainPhys Neuronal medium with SM1 supplement, then plated onto 35mm #1.5 glass-bottom dishes (MatTek Life Sciences) or 12mm circular #1.5 coverslips (Neuvitro) coated with polyethylenimine (100 μg/ml; Polysciences). Neurons were incubated in 5% CO2 at 37 °C, with half media change every four days.

Immunofluorescence staining

Neurons plated on coverslips were rinsed with sterile Hank's Balanced Salt Solution (HBSS) and fixed for 10min with pre-warmed 4% paraformaldehyde (PFA) (Electron Microscopy Sciences) in phosphate buffered saline (PBS). Fixed neurons were rinsed three times with PBS and permeabilized in 0.1% Triton X-100 (Millipore Sigma) in PBS for 10min. Neurons were then incubated in blocking buffer containing 5% bovine serium albumin (BSA) and 5% Normal Goat Serum (Jackson ImmunoResearch) for 30min, and labeled with primary antibodies diluted in PBS containing 0.1% normal goat serum overnight in 4 °C. The following day, neurons were washed three times in PBS, stained with secondary antibody for one hour, and washed three times with PBS. DNA was stained using Hoechst 33342 (1:10000 in PBS) for 5 minutes. Cells were washed twice with PBS and mounted in ProLong gold antifade mountant (ThermoFisher) for confocal or ProLong glass antifade mountant for SIM. For timecourse experiments, coverslips of neurons derived from the same animal were fixed at different timepoints. Coverslips fixed on earlier timepoints were stored in PBS at 4 °C until the end of the timecourse. Once all coverslips were collected, they were stained and mounted simultaneously. Primary antibodies used for fluorescence imaging in this study are as follows: mab414 (anti-FG-Nups; Abcam 24609, 1:800 dilution), anti-Nup210 (Bethyl Laboratories A301-795A, 1:200), anti-Nup153 (Abcam 96462, 1:250), anti-Nup98 (Abcam 50610, 1:250), anti-Nup358 (Millipore Sigma ABN 1385, 1:200),

anti-LaminA/C (Cell Signaling 4777, 1:200), anti-Map2 (Novus Biologicals NB300-213, 1:1000).

HaloTag-Nup107 labeling

For visualization of HaloTag-Nup107 in Fig. 3, neurons were incubated in media containing 50nM JF646 HaloTag ligand[104] (Promega GA1120) or JFX554 HaloTag ligand[105] (Kind gift of L. Lavis, Janelia) for 30 minutes. Excess ligands were then washed out by incubating labeled cells twice in neuronal media for >1h. Cells were then fixed and immunostained with antibodies. For pulse-chase labeling in Fig. 4, DIV3 neurons plated on glass coverslips were incubated in media containing 50nM JFX554 HaloTag ligand overnight. On DIV4, coverslips were rinsed with HBSS, incubated in neuronal media twice for 1h each to wash out excess ligand, then rinsed again with HBSS. At least one coverslip was fixed to establish DIV4 NPC density. Remaining coverslips were incubated in conditioned neuronal media containing 50nM JF646 HaloTag ligand. Coverslips were subsequently washed and fixed on DIV6, 8, and 10. On DIV7, half of media was replaced with fresh conditioned media containing 50nM JF646. Conditioned neuronal media was generated by collecting media from excess neurons of the same age and combining 1:1 with fresh neuronal media. After DIV10, all fixed coverslips were immunostained with anti-Nup153 primary antibody and Alexafluor 488-conjugated secondary antibody to label total NPC population. For DIV10-18 pulse-chase, DIV9 neurons were labeled overnight with 50nM JFX554 HaloTag ligand (pulse) followed by washout on DIV10. At least one coverslip was fixed on DIV10, and the rest were cultured in media containing 50nM JF646 ligand (chase) until DIV18, at which point they were washed and fixed. Fixed coverslips were immunostained with anti-Nup358 antibody and Alexafluor 488-conjugated secondary antibody.

Preparation and labeling of cortical brain tissue sections

Brains were dissected from P0 and P14 mouse pups that were transcardially perfused with 4% paraformaldehyde, post-fixed in 4% paraformaldehyde for 24 hrs, and cryoprotected in 20% sucrose for 24 hrs. 20 μm brain sections were prepared on a cryostat, adhered to charged slides, and dehydrated. Brain sections were washed with 0.01% PBS, permeabilized for 1.5 hours with PBS containing 0.1% Triton-X-100, and incubated for 20 hrs with 1μM JFX650 in PBS containing 0.1% Triton-X-100. Labeled sections were washed with several changes of PBS containing 0.1% Triton-X-100, stained with Hoechst (1:10000), rinsed with PBS, and cover slipped with Prolong Glass mounting medium.

dSTORM sample preparation and imaging

Neurons were rinsed with sterile HBSS and fixed for 10min with pre-warmed 4% PFA (Electron Microscopy Sciences) in PBS. Following fixation, neurons were rinsed three times with PBS and permeabilized in 0.2% Triton X-100 (Millipore Sigma) in PBS for 5min. Neurons were then incubated in blocking buffer containing 5% BSA for 30min, and labeled with Nup210 polyclonal antibody (Bethyl laboratories A301-795A; 1:200 in PBS) for two nights at 4 °C. Neurons were washed three times in PBS and stained with goat-anti-rabbit Alexa Fluor 647 Fab Fragment (1:800; Jackson ImmunoResearch 111-607-003) for an hour, washed three times with PBS, and imaged. Imaging and processing to determine localization and correct drift were conducted as previously described[106]. Samples were imaged in a

buffer containing 100mM Tris, 25mM NaCl, 10% glucose, 1% β-mercaptoethanol, 500 μg/ml glucose oxidase (Sigma) and 80 μg/ml catalase (Sigma). Images were rendered by generating 2D histograms from localizations followed by convolution with a Gaussian for display purposes.

Expansion microscopy

DIV10 neurons cultured on circular 12mm coverslips were fixed and immunostained with primary and secondary antibodies as described above. After the final wash following secondary antibody labeling, samples were incubated for 1h at room temperature in 25mM MA-NHS (methacrylic acid N-hydroxy succinimidyl ester) diluted in PBS[107] then washed three times in PBS. Gelling chamber was assembled by covering a glass slide with a layer of parafilm and using stacks of two #1.5 square coverslips as spacers placed 8mm apart, in a setup similar to what was previously described[108]. Each coverslip was flipped onto spacers neuron-side down and the resulting chamber was gently filled with U-ExM gelling solution on ice[109] (19% sodium acrylate, 10% acrylamide, 0.1% bis-acrylamide in PBS with 0.5% TEMED and 0.5% APS added last), then incubated in a humid container for 1h at 37 °C. Afterwards, gels was carefully isolated, digested with proteinase-K as in the U-ExM protocol, and allowed to expand for 30 minutes in a 6-well dish filled with ddH_2O. Subsequently, gels were each moved to a 10cm dish, exchanged twice with fresh ddH_2O, then allowed to expand overnight at 4 °C in fresh ddH_2O. Approximately 4x expansion was estimated based on the width of the expanded gel. Fully expanded gels were cut in pieces and mounted cell-side-down on glass-bottomed 60mm dishes coated with poly-L-lysine. Gels were covered with clean ddH_2O and imaged on ECLIPSE Ti inverted laser-scanning Nikon A1 confocal microscope with a 60x Apochromat water immersion (NA 1.2) objective using NIS-Elements AR (Nikon).

Microscopy

SIM imaging was conducted on a Nikon N-SIM microscope equipped with an sCMOS camera (Flash 4.0; Hamamatsu Photonics, Japan) and LU-NV laser unit (Nikon) using a 100x Apochromat oil objective (NA 1.49). Two-color SIM imaging was only conducted on Map2-positive neurons. Z-stack acquisitions were centered around the flat plane of the nuclear envelope (NE) facing the adherent surface of the coverslip. 9 optical sections for dual-color imaging (Alexafluor488 and Alexafluor555 immunofluorescence labeling) and 7 optical sections for triple-color imaging (JFX554, JF646, and Alexafluor488 immunofluorescence labeling) were obtained at 200nm intervals. For reconstruction from raw data, illumination modulation contrast was set at 1 and high-resolution noise suppression was set between 0.1 and 0.8. After reconstruction, two optical slices most perfectly situated in the flat NE plane were combined into maximum intensity projection for analysis. Confocal imaging was performed on ECLIPSE-Ti inverted laser-scanning Nikon A1 confocal microscope using an Apochromat Lambda 60x oil (NA 1.4, WD 0.13) objective, an ECLIPSE-Ti2 Nikon inverted microscope equipped with a spinning-disk scan head (Yokogawa, CSU-X1) and an EM-CCD camera (iXon Ultra 888) with an Apochromat TIRF 60x oil objective (NA 1.49), a Leica Stellaris 8 microscope with a HC PL APO 63x/1.40 CS2 oil objective, or a Leica Stellaris 5 microscope with a HC PL APO 63x/1.40 CS2 oil objective. Imaging was conducted using the Nikon NIS Elements software or the

Leica LAS X software at room temperature. All intensity measurements were performed on raw, unadjusted images. For presentation, images were adjusted for brightness and contrast. For experiments comparing fluorescence intensity, these adjustments were conducted using the same settings.

Western blot

Brains from P0 mouse pups were isolated into ice cold, filtered dissection buffer as with primary neuron isolation. Dissected cortices were placed into a microcentrifuge tube containing 100μL lysis buffer (RIPA (ThermoFisher; #89900) with cOmplete Mini Protease Inhibitor Cocktail (Roche; #11836153001)) and homogenized using a plastic plunger followed by pipetting with a P200 pipet tip. Samples were spun down at 15,000 g and supernatants were collected. Pierce BCA protein assay (ThermoFisher; #23227) was performed to determine protein concentration and lysates were normalized to 1 μg/μL with lysis buffer. Normalized lysates were mixed with sample-loading buffer (Invitrogen NP0007) containing 2-mercaptoethanol (80μL added to 920μL sample-loading buffer) and boiled for 5 min at 95°C. 7.5 μg of protein and Precision Plus Kaleidoscope protein standard (Bio-Rad #1610375) were loaded and run on 4–12% Bis-Tris gels (Invitrogen NP0323PK2). Protein was then transferred (350 mA for 1 hr at 4°C) onto a 0.22 μm PVDF membrane in transfer buffer containing 20% methanol. Membranes were blocked in 5% non-fat dry milk in TBS-T (Tris-buffered saline (TBS) with 0.1% Tween-20), washed once in TBS-T, and cut horizontally at the 75kDa mark. Membranes were incubated in TBS-T containing primary antibodies overnight at 4°C. Top half was incubated in anti-Nup107 (1:1000; ab236634) and HaloTag (1:500; Promega G9211). Bottom half was incubated in anti-GAPDH (1:1000, MAB374) and anti-β-actin (1:1000, Cell Signaling 4967) The next day, membranes were washed three times with TBS-T, incubated 1h at room temperature in secondary antibodies, then imaged using Odyssey CLx. Donkey anti-mouse 680 and donkey anti-rabbit 800 IR secondaries were used at 1:10,000 dilution in 1:1 mixture of TBS-T and Intercept (TBS) Blocking buffer (LICOR 927-60000) containing 0.01% Tween-20.

Transmission electron microscopy

Primary neurons were cultured on 35mm MatTek glass bottom dishes. For pre-fixation, cells were incubated in 1.25% glutaraldehyde in 0.05M cacodylate buffer at 37 °C for 5 minutes then 4°C overnight. Cells were post-fixed in a mixture of 1% osmium tetroxide (OsO_4) and 1% potassium ferrocyanide [$K4Fe(CN)_6$] in 0.1M cacodylate buffer. For improved contrast of the subcellular structures, the pre- and post-fixed cells were stained with 1% thiocarbohydrazide, additional 1% OsO4, 1% uranyl acetate, and Walton’s lead aspartate. Cells were dehydrated in ethanol, infiltrated in Spurr's resin, and thermally polymerized at 70°C for 48 hours. A Leica EM UC7 ultramicrotome was used to cut 70nm ultrathin serial sections and the sections were placed on 300 mesh Cu bare grids. Sections were coated with 4nm carbon by a Leica EM ACE600 high vacuum coater, observed under a JEOL JEM-1400 Plus LaB6 transmission electron microscope at 60keV high tension, and imaged by an AMT NanoSprint 12 CMOS camera.

Scanning transmission electron microscopy tomography

To reconstruct 3D representations of specimens, a high voltage transmission electron microscope (Titan Halo, 300kV; Thermo Fisher Scientific) was operated in scanning mode, enabling us to image thick sample sections (~750nm). The sections were cut from a resin-embedded material processed for electron microscopy as described above, and then placed on 50nm Luxel film slot grids. After the grids were glow-discharged on both sides, gold particles of different size (10nm, 20nm and 50nm) were deposited on the sample surfaces for alignment purpose. The specimen under interest was tilted from −60° to +60° every 0.5° at four evenly distributed azimuthal angle positions as previously described[110] and micrographs were collected on an annular dark field detector. Data acquisition was performed with SerialEM (version 3.6.12) at magnifications corresponding to pixel sizes in the range of 0.5nm to 2.5nm at full resolution. An iterative reconstruction procedure[110] was used to reconstruct the final volumes. Segmentation and animations were generated manually using 3dmod software (version 4.11.7; University of Colorado Boulder, Boulder, CO, USA).

Determination of nucleoporin puncta localization and density

Nuclear ROIs were traced manually in FIJI[111]. For each image, a binary mask of ROIs was generated and saved. For images with high background signal (i.e. Nup antibody-labeled images), min/max histograms were adjusted on FIJI such that Otsu thresholding excluded nonspecific background signal. MATLAB scripts were used to obtain coordinates of nucleoporin puncta. First, all masks were eroded by 15px to exclude the nuclear rim where the nuclear envelope starts to curve, then overlayed with corresponding images after Otsu-thresholding. Then, imextendedmax (extended-maxima transform) was used on individual nuclei from these images to identify peaks of nucleoporin puncta. The x-y coordinate of each peak was recorded. If the peak of a puncta spanned two or more pixels, the centroid was used as the coordinate. Puncta density was calculated by dividing the number of unique peaks by the area of the eroded nuclear ROI. Outputs from the thresholding and masking step and images of unique peaks were saved as .tif files to enable visual inspection of proper peak identification.

Autocorrelation analysis of dSTORM and SIM data

For dSTORM images, pair auto-correlations were tabulated from localizations within a user-defined mask, as described previously[106]. For SIM images, pair auto-correlations were tabulated from images with a user-defined mask, as described previously[112]. In some panels, curves are normalized to the value of the first spatial bin (corresponding to r<30nm) as normalized $g(r) = 1+(g(r)-1)/(g(r<30nm)-1)$. In all cases, curves shown represent the average over cells with errors indicating the SEM over cell measurements.

Nearest neighbor distance analysis from SIM images

The nearest neighbor distance between nucleoporin puncta and the number of puncta within a specified radius were calculated in MATLAB using the knnsearch() and rangesearch() functions, respectively.

Nucleoporin puncta colocalization

Colocalization of puncta was determined based on assessment of whether peaks from one channel (“query”) overlay with the thresholded puncta of the other channel (“search”) using a custom written function. To determine % colocalization between Nup153 and HaloTag-Nup107, an image of unique peaks from the “query” channel were overlayed with the thresholded image of the “search” channel and the % of peaks whose coordinate’s pixel value in the “search” channel image is >0 was calculated. To determine the density and coordinates of new JF646 puncta in the HaloTag pulse-chase experiment, this method was adapted such that JF646 peaks that did not colocalize with JFX554 puncta were counted.

Nuclear rim fluorescence intensity measurement of Nups

For each nucleus, the z-plane that most closely represented the middle plane of the nucleus was manually determined and an ROI of the nuclear rim was manually traced in FIJI. Using a custom-written script, ROIs was converted into 4px-wide bands containing only the nuclear periphery, which were then used to measure the fluorescence intensity of nucleoporins at the nuclear rim. Only Map2-positive neurons were analyzed. For visualization, fluorescence intensity of each cell was normalized to the average intensity of the reference timepoint. For statistics, log of all raw intensity values were calculated to preserve the variability in the dataset, which is lost with normalization. Average log(intensity) values were calculated for biological replicates and used to compare timepoints.

NE bleb analysis

TEM images were acquired such that one entire nucleus and associated NE blebs (if applicable) were visible per image. Upon imaging all coverslips, all folders and files were blinded such that genotype and neuronal age identifiers were removed. All nuclei were analyzed for 1) presence of blebs and 2) number of blebs. Number of blebs was determined by counting structures that fit the following criteria: 1) a clear bleb “neck” that connects to the inner nuclear membrane and is enveloped by the outer nuclear membrane, or 2) a membrane-bound vesicle-like structure directly adjacent to the nuclear membrane that is enveloped by the outer nuclear membrane. Note that this method of blinded quantification consistently undercounts NE blebs by excluding all structures that appear like double-membrane vesicles, which are visible portions of blebs whose connection to the inner nuclear membrane occurs on a different plane from the imaging plane. Following quantification, images were unblinded and grouped by biological replicate for processing.

STEM pore dimension analysis

To assess the dimensions of a pore assembly found in electron tomograms, the octagonal structure of the pore was segmented by placement of eight points on the nuclear side. Segmentation was done separately for each pore using the following steps: A small sub-volume containing the pore was first extracted from the full tomogram, and a preliminary segmentation of eight corner points was placed manually. Principal component analysis using the eight points was conducted to determine the octagon orientation, and the sub-volume was re-sliced to orient the pore in a front-facing view. The segmentation was

then refined by readjusting the corner points and re-slicing the sub-volume. This process was iterated until a satisfactory segmentation of the pore was achieved. The final resliced sub-volumes, in which a pore assembly is mostly represented in its intrinsic reference frame, were stored. A blinded analysis on those sub-volumes was then conducted to assess the possible presence of a dense plug in the pore channel. The entire set, extracted from the available tomograms from both WT and torsinA-KO neurons, was shuffled and assigned a random ID prior to the analysis. Randomized sub-volumes were then scored manually for the presence of a dense central plug. Randomization and blinded quantitation were performed by independent investigators. For pore dimension analysis, the diameter of each pore was calculated as $d / sin(\pi/8)$ where d represents the average distance between two adjacent corner points of the segmented pore octagon. Segmentation was carried out with the 3dmod software.

NPC segmentation from dSTORM

Individual NPCs were segmented through a multi-step and fully automated process designed to identify objects of a particular size and aspect ratio while not biasing towards particles with distinct pores. First, an initial segmentation was conducted using a home-built implementation of DBSCAN[106,113], with ε=40 nm and minPts = 25. The size of the major and minor axes of segmented objects were then determined by tabulating the eigenvalues of the covariance of x,y points with each segment. Single pores were defined as segments with major axes between 33 and 53nm, and minor axes between 23 and 43nm. For DBSCAN objects with major and minor axes larger than this range, we further segmented pores as follows: Images were reconstructed from points with 5nm bin sizes, then blurred with a disk-shaped filter with radii corresponding to 70nm. Local maxima were then identified in filtered images, then culled to remove maxima less than 90nm apart. Localizations acquired within 80nm of the remaining local maxima were associated as candidate particles. Candidate particles were retained if their major and minor axes met the same criteria as used in the initial DBSCAN segmentation.

Segmented pores were aligned using algorithms described previously[114]. To speed computation and estimate errors, localizations for a randomly chosen subset (250) of segmented pores were inputted into the alignment algorithm using 100nm pixels as units, with the “scale” parameter set to 10nm (0.1 in 100nm units). The final step was accomplished with imposed 50-fold symmetry to generate an angularly symmetric super particle. The density functions were tabulated by calculating the radial distance of super-particle localizations from the center of the particle, then binning to make a histogram, using bin-widths of Δr=2.5nm and each bin was divided by the total number of localizations in the super-particle, to correct for systematic differences in imaging conditions across conditions. Histograms were further divided by the area associated with each bin = $2\pi r\Delta r$ to obtain the normalized localization density at each radius. For each super-particle, the radius associated with the maximum localization density was estimated by fitting normalized histograms to a 2nd order polynomial between 25 and 55nm, then returning the maximum of the fit. Significance between conditions was determined using a 2-tailed t-test of bootstrapped replicates through the ttest2 function in MATLAB.

Super-particles generated from WT DIV18 nuclei were used to validate the segmentation procedures used. NPCs in these nuclei can be densely distributed, leading to some particles segmented as large clusters in the initial DBSCAN segmentation.

Calculation of nearest neighbor distances from dSTORM segmented NPCs

The centroids from each segmented NPC were determined by averaging the x and y coordinates of all localizations in the segmented NPC particle. Nearest neighbor distances were determined by tabulating pairwise distances between all NPC centroids with a cutoff of 1μm using the crosspairs_indicies() function in https://github.com/VeatchLab/smlm-analysis, then extracting the shortest distance associated with each NPC.

Data analysis and visualization

Statistical information, including n (total cells analyzed), mean, and statistical significance values, is indicated in the figures or figure legends. Data are plotted using superplots[115] when applicable. N (number of biological replicates) is represented in superplots and statistical tests were performed on means of biological replicates. At least three biological replicates were used per experiment. Statistical tests were determined upon consultation with CSCAR (Consulting for Statistics, Computing, and Analytics Research) at the University of Michigan. Sphericity was assumed for ANOVA tests based on the Mauchly's test of sphericity, which failed to reject the null hypothesis. Statistical significance was determined with Graphpad Prism 10 using the tests indicated in each figure. Data were considered statistically significant at *P < 0.05, **P < 0.01, ***P < 0.001 and ****P < 0.0001.

Statistics and Reproducibility

No statistical tests were used to determine the sample size. No data were excluded from analysis. Data from TEM and STEM experiments were randomized and quantitated by a blinded investigator. All other experiments were not randomized.

Extended Data

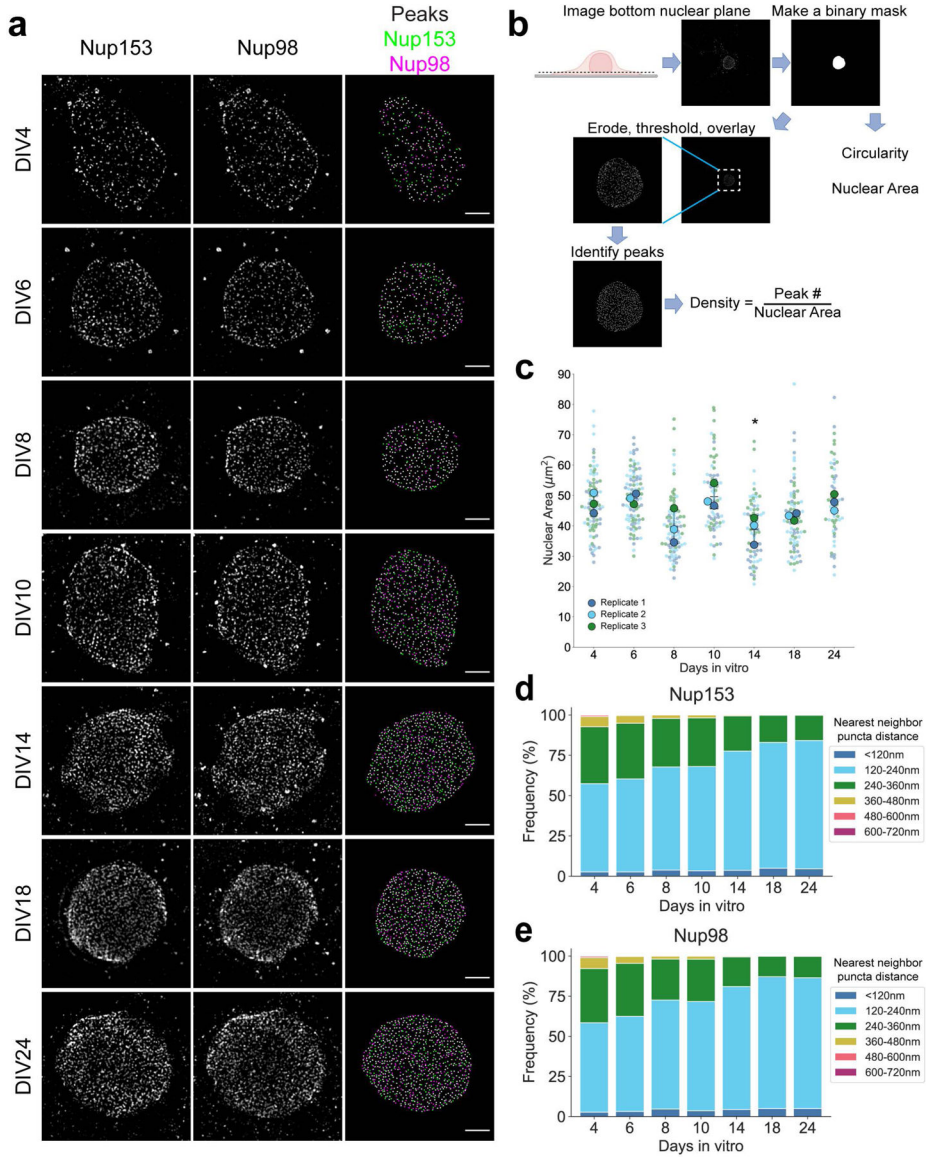

Extended Data Figure 1: Identification and analysis of nucleoporin puncta

a, SIM images of primary neurons aged DIV4, 6, 8, 10, 14, 18 and 24 labeled with anti-Nup153 and anti-Nup98 antibodies. Peaks column shows peaks identified from Nup153 (green) and Nup98 (magenta) puncta. Scale bar = 2μm.

b, Schematic of image analysis pipeline. The flattest part of the nuclear envelope was imaged. Nuclear ROIs were determined by manually outlining each nucleus. ROIs were eroded to account for nuclear envelope curvature at the edge, then overlayed onto Otsu thresholded images. Local maxima were identified with extended-maxima transform and used to establish peaks corresponding to each Nup.

c, Superplots of nuclear ROI area as determined by Nup153/Nup98 staining in maturing neurons aged DIV4, 6, 8, 10, 14, 18 and 24. Plots show mean ±SD, with color coding indicative of biological replicates. One-way ANOVA with Dunnett's multiple comparisons

test on 3 biological replicates was performed, with DIV4 as the reference condition. Only DIV14 showed statistical significance; *P=0.0331.

d, e, Frequency distribution of nearest neighbor distances of Nup153 (**d**) and Nup98 (**e**) puncta. For each Nup153 and Nup98 peak, the distance to its nearest neighbor was calculated. The results from three biological replicates were combined for each timepoint.

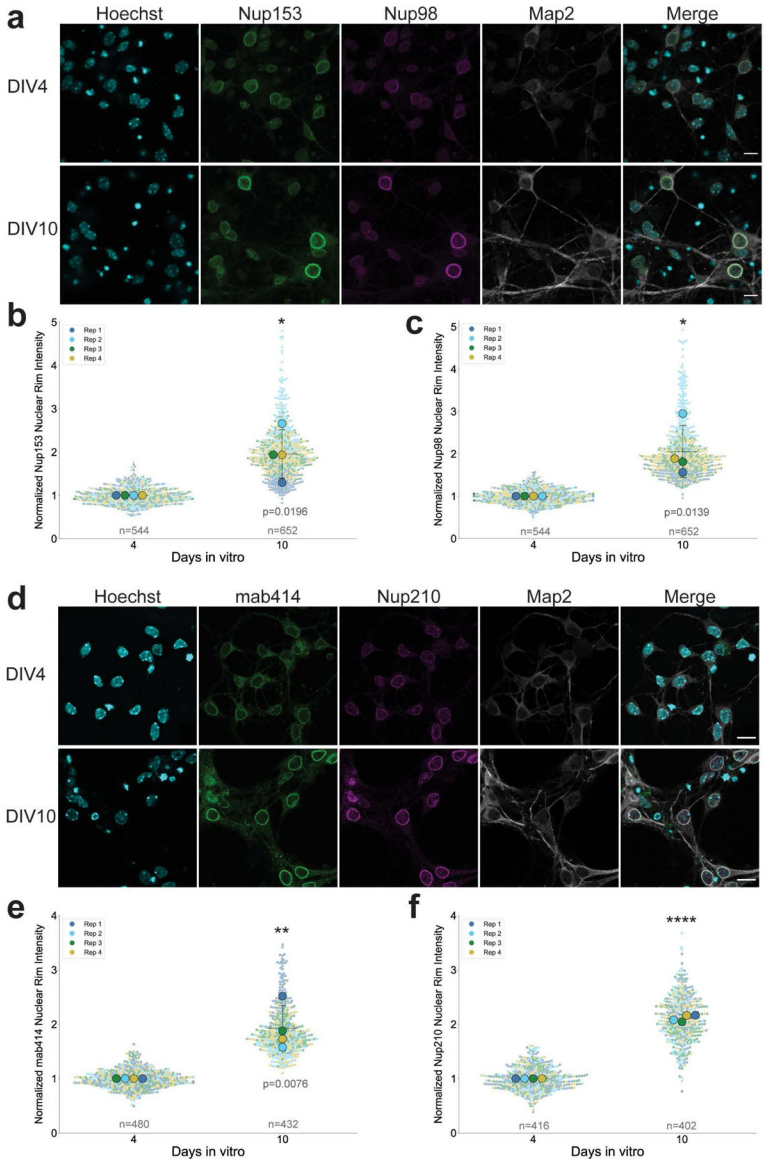

Extended Data Figure 2: Multiple NPC components exhibit density increase during neuronal maturation

a, Confocal images of DIV4 and DIV10 primary neurons labeled with anti-Nup153 and anti-Nup98 antibodies. Scale bar = 10μm.

b, c, Normalized nuclear rim fluorescence intensity of Nup153 and Nup98 in DIV4 and DIV10 primary neurons. Plots show mean ± SD, with color coding indicative of biological replicates. *P=0.0196 (**b**), *P=0.0139 (**c**) using two-tailed paired t-test from 4 biological replicates.

d, Confocal images of DIV4 and DIV10 primary neurons labeled with anti-FG nucleoporin (mab414) and anti-Nup210 antibodies. Scale bar = 10μm.

e, f, Normalized nuclear rim fluorescence intensity of FG-Nups (mab414) and Nup210 in DIV4 and DIV10 primary neurons. Plots show mean ± SD, with color coding indicative of biological replicates. **P=0.0076 (**e**), ****P<0.0001(**f**), two-tailed paired t-test from 4 biological replicates.

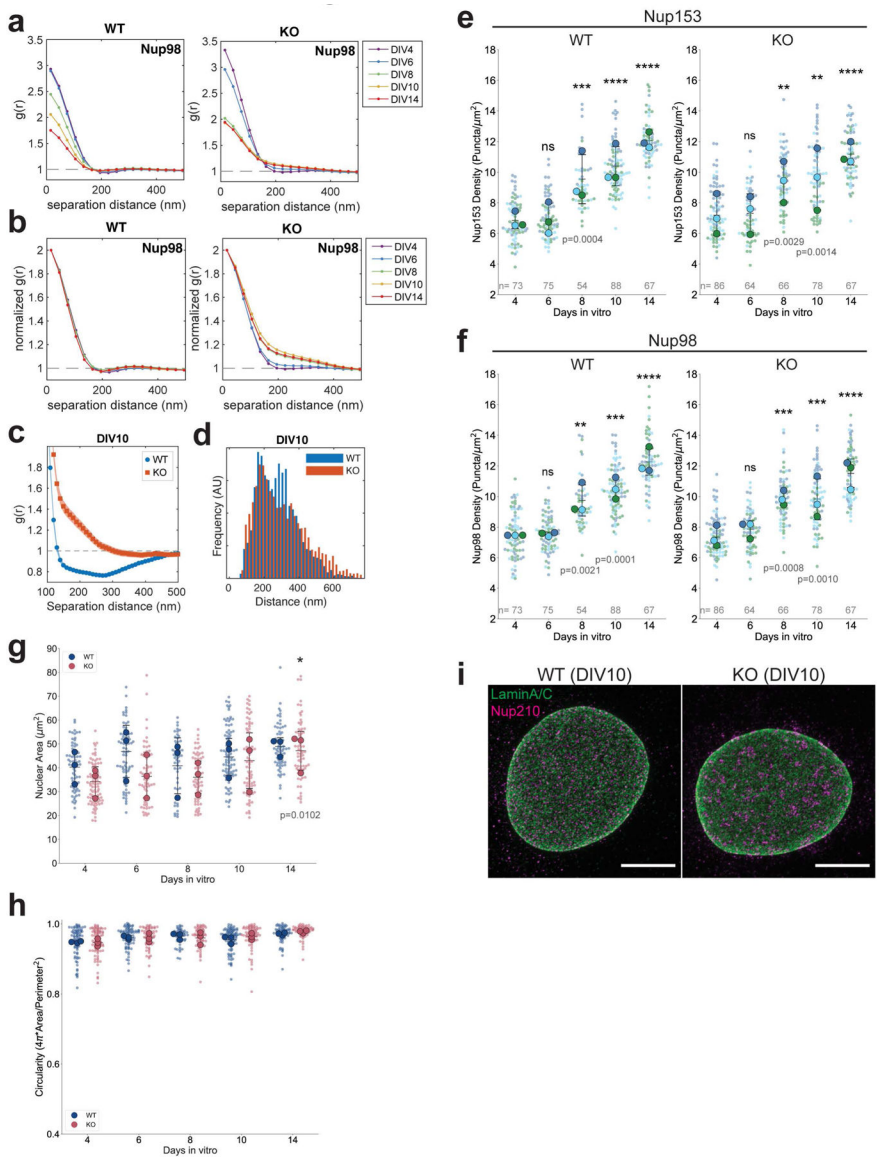

Extended Data Figure 3: Comparison of WT and torsinA-KO neuronal NPC spatial organization and nuclear morphology

a, Autocorrelation plot of WT and torsinA-KO neurons calculated from Nup98 WT and torsinA-KO SIM images.

b, Normalized autocorrelation plot of WT and torsinA-KO neurons calculated from Nup98 WT and torsinA-KO SIM images. Autocorrelations were normalized to account for amplitude dependency on NPC density.

c, Autocorrelation plot of DIV10 WT and torsinA-KO neurons calculated from Nup210 dSTORM images.

d, Nearest neighbor distance of segmented DIV10 WT and torsinA-KO NPC centroids.

e, f, WT and torsinA-KO Nup153 (**e**) and Nup98 (**f**) puncta density in maturing primary neurons aged DIV4, 6, 8, 10, 14. Plots show mean ± SD, with color coding indicative of biological replicates. Timepoints from the same biological replicate were matched. Repeated measures two-way ANOVA with Dunnett's multiple comparisons test was performed on 3 biological replicates, with DIV4 as the reference condition. ns, non-significant; P values are reported on the plots. ****P<0.0001; repeated measures two-way ANOVA with Dunnett's multiple comparisons test, using DIV4 as a reference, 3 biological replicates.

g, Nuclear area of WT and torsinA-KO neurons calculated from manually drawn ROIs from SIM images. Plots show mean ± SD. Repeated measures two-way ANOVA with Sidak's multiple comparisons test was used to compare genotypes at each timepoint, and no comparisons reached statistical significance. Repeated measures two-way ANOVA with Dunnett's multiple comparisons test was used to compare all timepoints to DIV4 within each genotype, and only torsinA-KO DIV4 versus DIV14 reached significance (*P=0.0102).

h, Nuclear ROI circularity of WT and torsinA-KO neurons calculated from manually drawn ROIs from SIM images. Plots show mean ± SD. Repeated measures two-way ANOVA with Sidak's multiple comparisons test was used to compare genotypes at each timepoint. No statistical significance was detected.

i, Expansion microscopy of DIV10 WT and torsinA-KO neurons labeled with Nup210 and Lamin A/C antibodies. Representative images from 3 biological replicates per genotype are shown. Scale bar = 20μm.

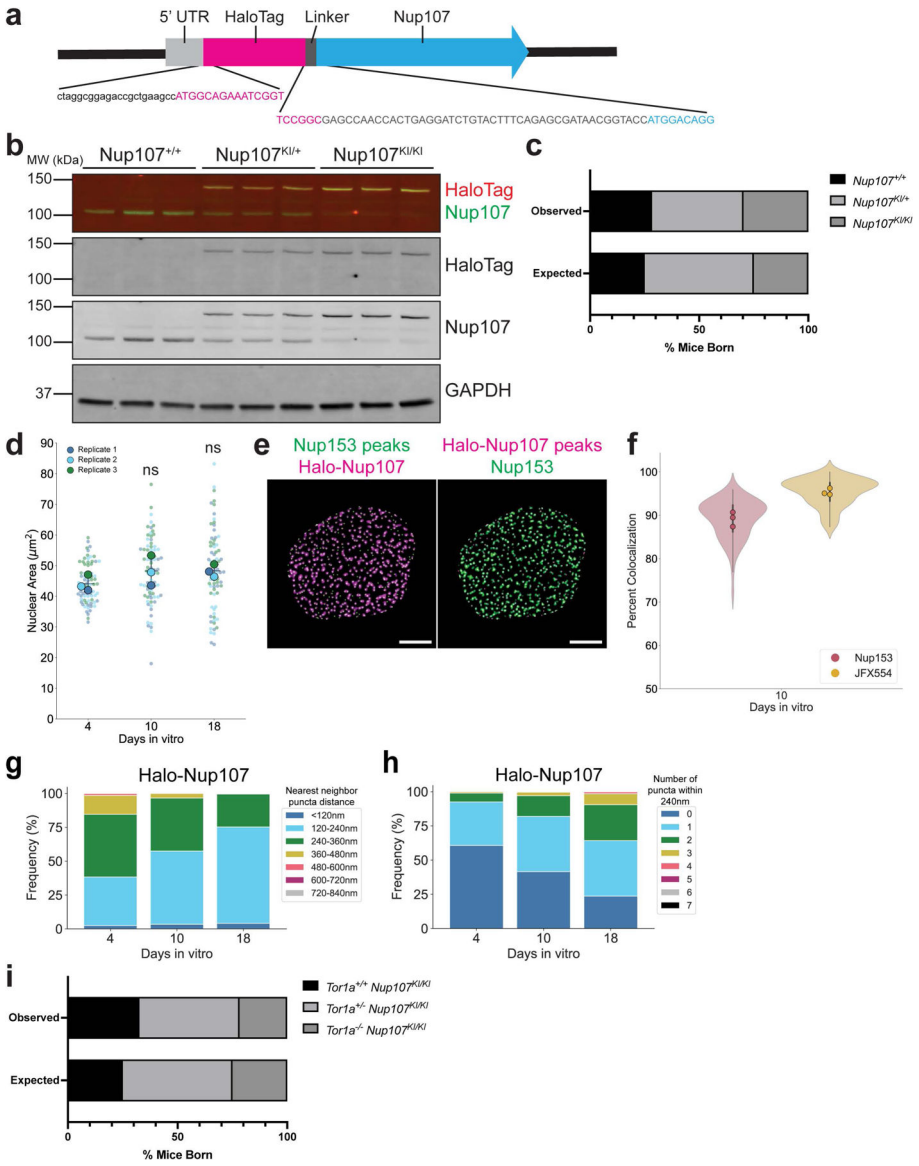

Extended Data Figure 4: Validation of HaloTag-Nup107 mouse line

a, Schematic of HaloTag-Nup107 fusion, including 5' untranslated region (UTR, light grey), HaloTag open reading frame (magenta), flexible linker (dark grey), and Nup107 coding sequence (cyan).

b, Immunoblot of P0 cortical lysates from *Nup107*$^{+/+}$, *Nup107*$^{KI/+}$, and *Nup107*$^{KI/KI}$ mice probed with anti-Nup107 and anti-HaloTag antibodies. GAPDH was blotted as a loading control. Each band represents an independent biological sample (3 animals each).

c, Distribution of genotypes in litters derived from intercrossing *Nup107*$^{KI/+}$ mice. No deviation from the expected Mendelian ratio was observed (P=0.3729, Chi-squared test). 74 pups from 9 litters were analyzed.

d, Superplots of nuclear ROI area from Nup153 and JFX554 SIM images. Plots show mean ± SD, with color coding indicative of biological replicates. ns, not significant; repeated

measures one-way ANOVA with Dunnett's multiple comparisons test on 3 biological replicates, with DIV4 as a reference condition.

e, Representative image of Nup153 and HaloTag-Nup107 colocalization in DIV10 HaloTag-Nup107 neurons from 3 biological replicates. Scale bar = 2 μm.

f, Violin plot showing the percent of Nup153 and JFX554 puncta that colocalize with JFX554 and Nup153, respectively, in DIV10 neurons. Nup153 colocalization with JFX554 was measured by calculating the % of Nup153 peaks that overlap with thresholded JFX554 puncta, and vice versa.

g, Frequency distribution of nearest neighbor distances of JFX554 puncta. For each JFX554 peak, the distance to its nearest neighbor was calculated. Results from three biological replicates were combined.

h, Frequency distribution of JFX554 puncta within two-pore diameter (240nm) distance. For each JFX554 peak, the number of neighboring puncta within a radius of 240nm was calculated. Results from three biological replicates were combined.

i, Distribution of genotypes in litters derived from intercrossing *Tor1a*$^{+/-}$; *Nup107*$^{KI/KI}$ mice. All genotypes were born at the expected Mendelian ratio (P-0.4880, Chi-squared test). 46 pups from 6 litters were analyzed.

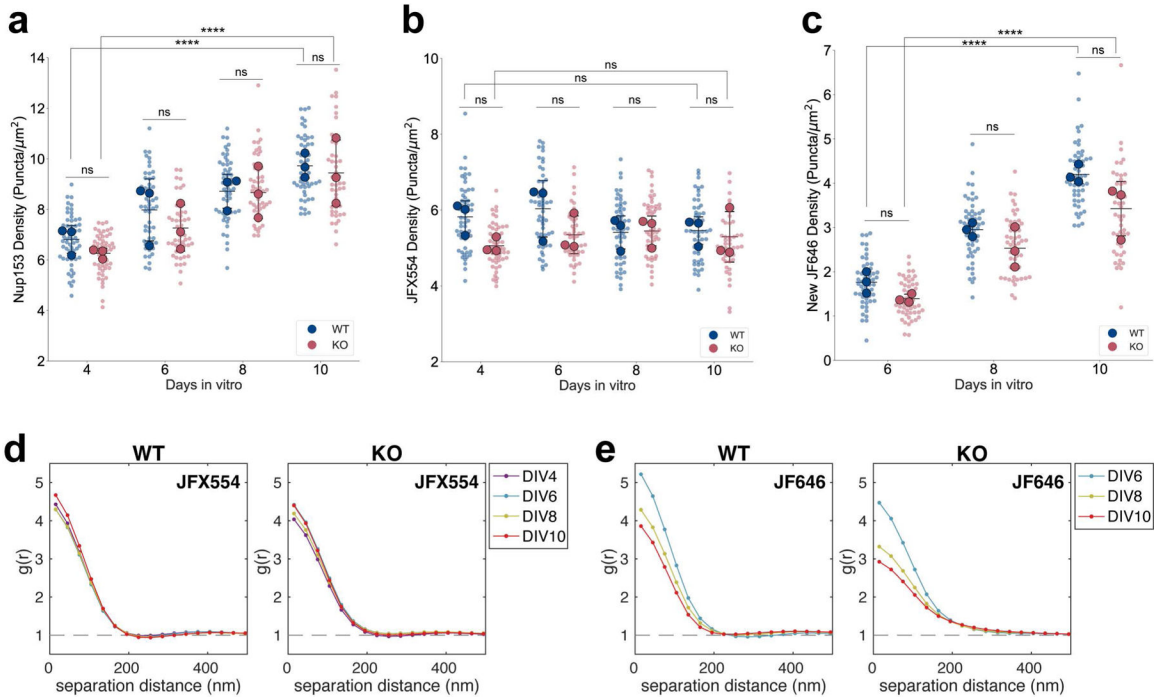

Extended Data Figure 5: Comparison of NPC density and distribution from HaloTag-Nup107 pulse-chase

a, b, c, Nup153 (**a**), JFX554 (**b**), and new JF646 (**c**) puncta density in maturing WT and torsinA-KO primary neurons aged DIV4, 6, 8, 10. Plots show mean ± SD from 3 biological replicates. Repeated measures two-way ANOVA with Sidak's multiple comparisons test was used to compare genotypes at each timepoint. No comparisons reached statistical significance. Repeated measures two-way ANOVA with Dunnett's multiple comparisons test was used to compare all timepoints to DIV4, with ****P<0.0001.

d, Autocorrelation of JFX554 images over 0–500nm separation distance. Similar starting amplitudes reflect constant JFX554 density.

e, Autocorrelation of JF646 images over 0–500nm separation distance. Decreasing starting amplitudes over neuronal maturation reflect increasing JF646 density. Broadening of the curve in torsinA-KO neurons indicates spatial correlation of NPCs over larger distances.

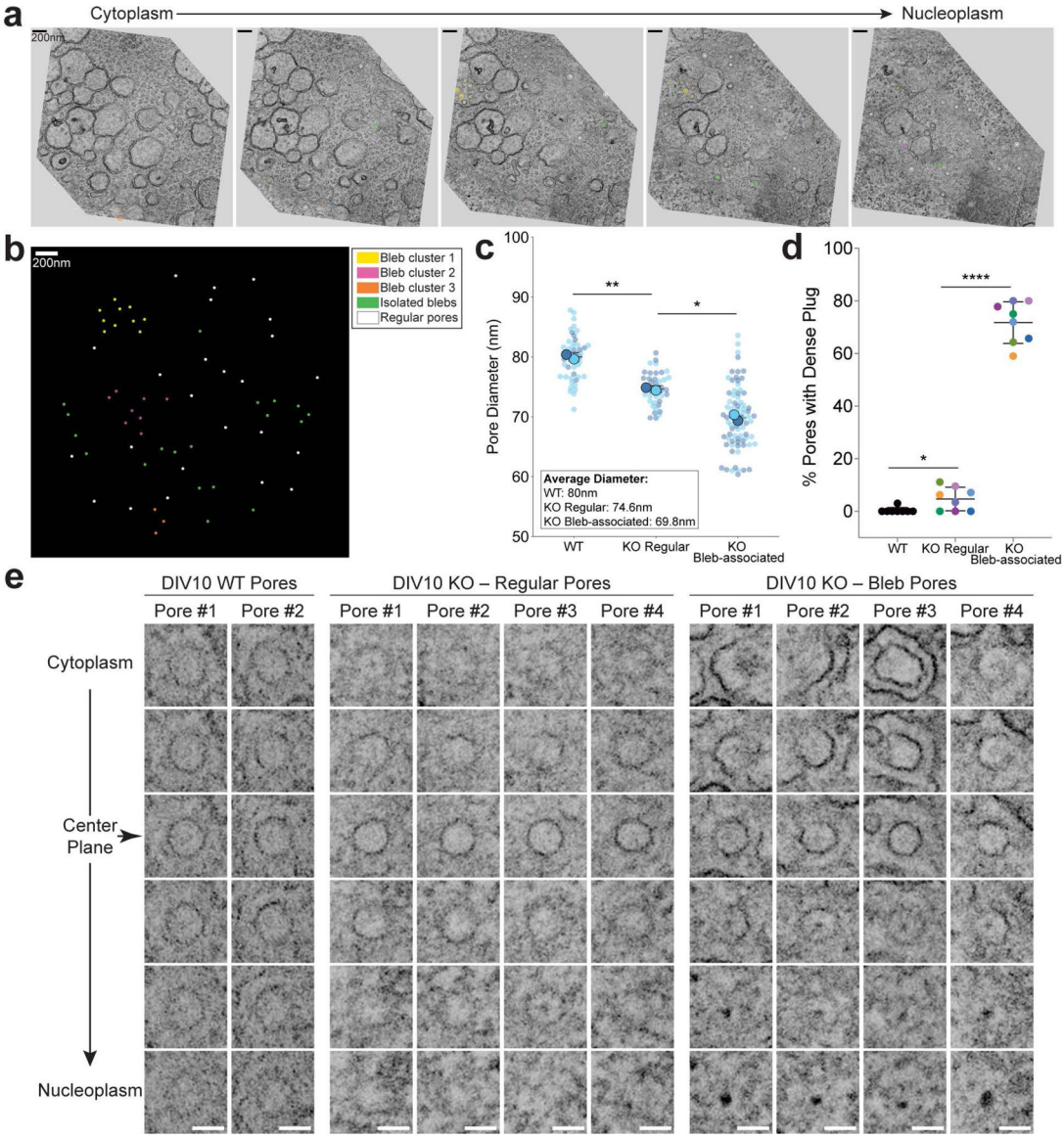

Extended Data Figure 6: Bleb-associated pores are narrow and exhibit nucleoplasmic central plugs

a, Slices from a DIV10 torsinA-KO tomogram oriented as an en-face view of the neuronal nuclear membrane. Pores at clusters of blebs, isolated blebs, or regular NPCs without blebs are marked by color-coded spheres centered around the middle plane of the pore channel, denoted by larger circles. Tomogram shown here is representative of 8 tomograms from two biological replicates.

b, Projection of all marked pores from the tomogram shown in (**a**).

c, Superplot of WT, KO regular (non bleb-associated), and KO bleb-associated pore diameter (nm). Plots show mean ± SD, with color coding indicative of biological replicates. Swarmplot of individual pore diameters (small points) is overlayed with the mean of pore diameters for each biological replicate (larger points). Pores from two WT and two torsinA-KO tomograms were analyzed. KO regular and bleb-associated pores were identified from the same torsinA-KO tomograms. *P=0.0128, **P=0.0068; two-tailed unpaired t-test from two biological replicates.

d, Blinded quantitation of the percentage of pores that have dense central plugs. Plots show mean ± SD with each point representing a cell. For KO regular and bleb-associated pores, points are color-coded to reflect quantitation from the same tomogram. Blinded quantitation was performed on 593 pores from 8 WT and 8 torsinA-KO tomograms obtained from two biological replicates each, with each tomogram from a different cell. *P=0.0302; two-tailed unpaired t-test with Welch's correction, ****P<0.0001 two-tailed paired t-test, using values from 8 tomograms.

e, Slices showing individual pores from DIV10 WT and torsinA-KO tomograms. Regular and bleb-associated torsinA-KO pores were sampled from the same tomogram. From top to bottom, the slices progress from the cytoplasmic side of the pore channel towards the nucleoplasm. Center plane of the pore channel is marked with a horizontal arrow. Scale bar = 100nm.

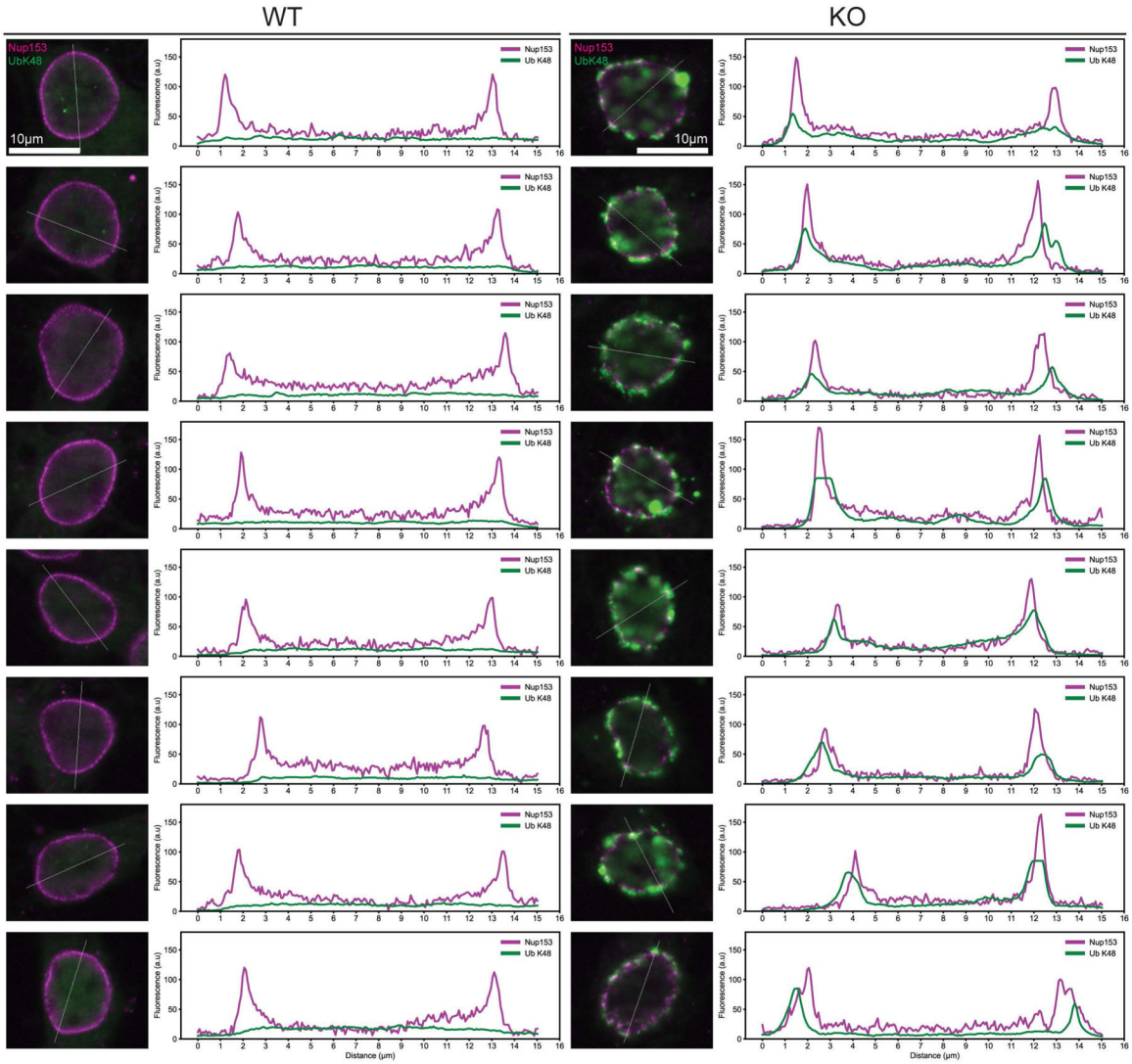

Extended Data Figure 7: NE blebs spatially correlate with NPC clusters

Line scan analyses of 8 WT and 8 torsinA-KO DIV10 nuclei from two biological replicates labeled with anti-Nup153 and anti-Ubiquitin-K48 antibodies.

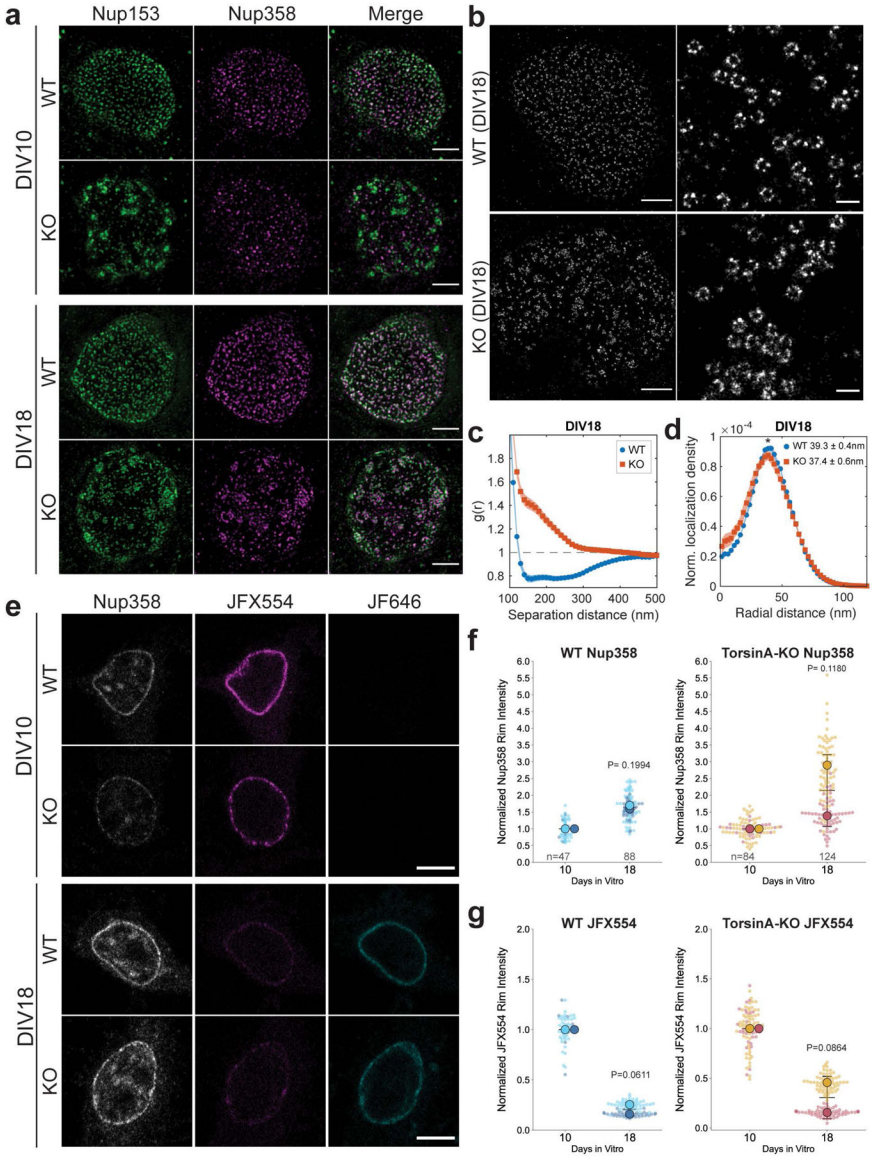

Extended Data Figure 8: Nup358 is recruited to persisting NPC clusters in DIV18 torsinA-KO neurons

a, SIM images of DIV10 and DIV18 WT and torsinA-KO neurons labeled with Nup153 and Nup358 antibodies. Scale bar = 2μm.

b, dSTORM images of Nup210 in DIV18 WT and torsinA-KO neurons. Scale bar = 2μm. Right panels show zoomed in view. Scale bar for right panels = 200nm.

c, Autocorrelation plot of DIV18 WT and torsinA-KO neurons, determined from Nup210 dSTORM images. 18 WT and 19 torsinA-KO cells from 3 biological replicates each were analyzed.

d, Normalized localization density along radial distance in averaged WT and torsinA-KO NPCs from DIV18 dSTORM images. Plots show mean ± SEM from eight bootstrapping rounds with 250 randomly selected pores each. *P=0.019.

e, Confocal images from DIV10-18 pulse-chase of WT and torsinA-KO neurons expressing HaloTag-Nup107. Scale bar = 5μm.

f, Plot of Nup358 nuclear rim fluorescence intensity from DIV10-18 pulse-chase. Plots show mean ± SD from two biological replicates with color coding to indicate replicates. All values were normalized to the mean DIV10 WT fluorescence intensity. Reported P values are from a two-way ANOVA test. “n” denotes the number of analyzed nuclei.

g, Plot of JFX554 nuclear rim fluorescence intensity from DIV10-18 pulse-chase. Plots show mean ± SD from two biological replicates with color coding to indicate replicates. All values were normalized to the mean DIV10 WT fluorescence intensity. Reported P values are from a two-way ANOVA test. Same number of nuclei were analyzed as in (**f**).

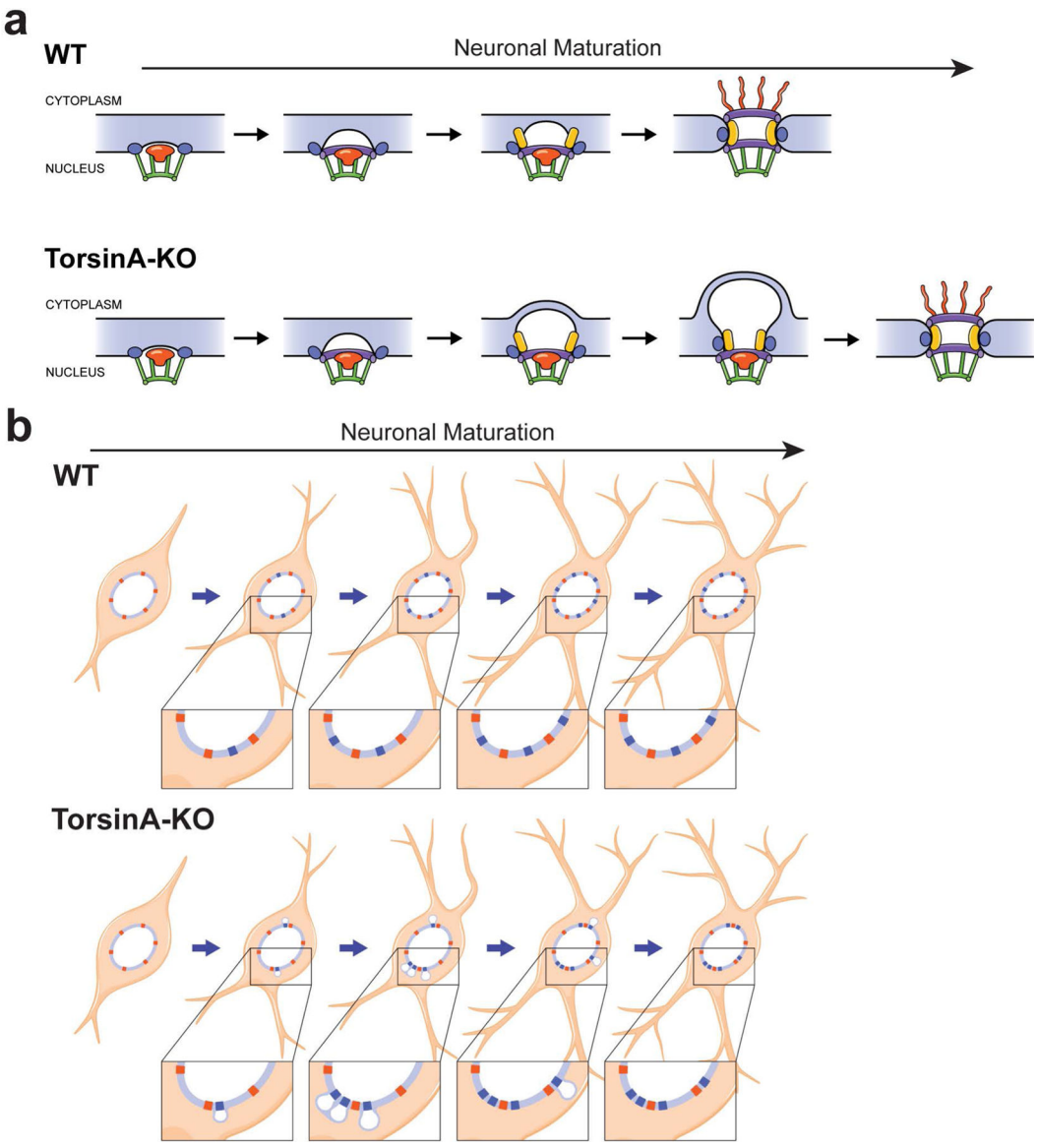

Extended Data Figure 9: Summary of the effects of torsinA loss on NPC spatial organization and dynamics

a, Model of interphase NPC assembly in WT and torsinA-KO neurons. Onset of NPC assembly is not affected by torsinA deletion. Nuclear basket, inner ring, and transmembrane nucleoporins are recruited to the nascent NPC as the INM starts to bud. Instead of the

normal INM-ONM fusion found in WT neurons, excessive INM extrusion causes NE blebs to emerge and enlarge in torsinA-KO neurons. These blebs stall torsinA-KO NPCs at an intermediate stage while NPC assembly completes in WT neurons. As torsinA-KO neurons continue to mature, NE blebs resolve and INM-ONM fusion occurs. Completion of NPC biogenesis is delayed in torsinA-KO neurons.

b, Model of NPC localization in maturing WT (top) and torsinA-KO (bottom) neurons. In WT neurons, newly forming NPCs (blue) localize to empty spaces between existing NPCs (red), thereby maintaining uniform spatial organization. In maturing torsinA-KO neurons, newly forming NPCs (blue) localize abnormally close to each other or to existing NPCs (red), causing aberrant clusters. NPC biogenesis is upregulated in both genotypes and total NPC number is not affected by the absence of torsinA.

Supplementary Material

Refer to Web version on PubMed Central for supplementary material.

Acknowledgements:

We thank the University of Michigan Microscopy Core facility, D. Levin and X. Li for animal husbandry, A. Taylor for assistance with MATLAB codes, S. Mosalaganti, A. Erwin, D. Boassa, and A. Moore for feedback and experimental discussions, A. Diehl for illustrations, H. Worman and D. Yellajoshyula for critical reviews. This work was supported by NIH R01 NS110853, R01 DK118480, R01 NS077730 to W.T.D., NIH R01 NS097542, R01 NS113943, R56 NS128110 to S.J.B., NIH GM129347 and NSF MCB1552439 to S.L.V, NIH T32 GM007315 and UM Rackham Predoctoral Fellowship to S.K., NIH U24 NS120055, 1S10OD021784, R01 GM082949 and NSF2014862-UTA20-000890 to M.H.E.

Data availability

STEM volumes are available on the Cell Image Library (http://www.cellimagelibrary.org/groups/57193). Numerical and western blot source data have been provided in Source Data. All other data supporting the findings of this study are available from the corresponding author on reasonable request.

References

1. Knockenhauer KE & Schwartz TU The Nuclear Pore Complex as a Flexible and Dynamic Gate. Cell 164, 1162–1171 (2016). [PubMed: 26967283]
2. Beck M & Hurt E The nuclear pore complex: understanding its function through structural insight. Nat. Rev. Mol. Cell Biol 18, 73–89 (2016). [PubMed: 27999437]
3. Coyne AN & Rothstein JD Nuclear pore complexes — a doorway to neural injury in neurodegeneration. Nat. Rev. Neurol 18, 348–362 (2022). [PubMed: 35488039]
4. Cho UH & Hetzer MW Nuclear Periphery Takes Center Stage: The Role of Nuclear Pore Complexes in Cell Identity and Aging. Neuron 106, 899–911 (2020). [PubMed: 32553207]
5. Kandel ER The Molecular Biology of Memory Storage: A Dialogue Between Genes and Synapses. Science 294, 1030–1038 (2001). [PubMed: 11691980]
6. Cohen S & Greenberg ME Communication Between the Synapse and the Nucleus in Neuronal Development, Plasticity, and Disease. Annu. Rev. Cell Dev. Biol 24, 183–209 (2008). [PubMed: 18616423]
7. Karpova A et al. Encoding and Transducing the Synaptic or Extrasynaptic Origin of NMDA Receptor Signals to the Nucleus. Cell 152, 1119–1133 (2013). [PubMed: 23452857]

8. Kaushik R, Grochowska KM, Butnaru I & Kreutz MR Protein trafficking from synapse to nucleus in control of activity-dependent gene expression. Neuroscience 280, 340–350 (2014). [PubMed: 25230285]
9. Sutton MA & Schuman EM Local translational control in dendrites and its role in long-term synaptic plasticity. J. Neurobiol 64, 116–131 (2005). [PubMed: 15883999]
10. Sutton MA & Schuman EM Dendritic Protein Synthesis, Synaptic Plasticity, and Memory. Cell 127, 49–58 (2006). [PubMed: 17018276]
11. Jung H, Gkogkas CG, Sonenberg N & Holt CE Remote Control of Gene Function by Local Translation. Cell 157, 26–40 (2014). [PubMed: 24679524]
12. Batista AFR & Hengst U Intra-axonal protein synthesis in development and beyond. Int. J. Dev. Neurosci 55, 140–149 (2016). [PubMed: 26970010]
13. Holt CE, Martin KC & Schuman EM Local translation in neurons: visualization and function. Nat. Struct. Mol. Biol 26, 557–566 (2019). [PubMed: 31270476]
14. Grima JC et al. Mutant Huntingtin Disrupts the Nuclear Pore Complex. Neuron (2017) doi:10.1016/j.neuron.2017.03.023.
15. Pappas SS, Liang CC, Kim S, Rivera CAO & Dauer WT TorsinA dysfunction causes persistent neuronal nuclear pore defects. Hum. Mol. Genet 27, 407–420 (2018). [PubMed: 29186574]
16. Eftekharzadeh B et al. Tau Protein Disrupts Nucleocytoplasmic Transport in Alzheimer's Disease. Neuron (2018) doi:10.1016/j.neuron.2018.07.039.
17. Coyne AN et al. G4C2 Repeat RNA Initiates a POM121-Mediated Reduction in Specific Nucleoporins in C9orf72 ALS/FTD. Neuron 107, 1124–1140.e11 (2020). [PubMed: 32673563]
18. Lin Y-C et al. Interactions between ALS-linked FUS and nucleoporins are associated with defects in the nucleocytoplasmic transport pathway. Nat. Neurosci 24, 1077–1088 (2021). [PubMed: 34059832]
19. Basel-Vanagaite L et al. Mutated nup62 causes autosomal recessive infantile bilateral striatal necrosis. Ann. Neurol 60, 214–222 (2006). [PubMed: 16786527]
20. Harrer P et al. Recessive NUP54 Variants Underlie Early-Onset Dystonia with Striatal Lesions. Ann. Neurol 93, 330–335 (2023). [PubMed: 36333996]
21. Savas JN, Toyama BH, Xu T, Yates JR & Hetzer MW Extremely Long-Lived Nuclear Pore Proteins in the Rat Brain. Science 335, 942–942 (2012). [PubMed: 22300851]
22. Toyama BH et al. Identification of Long-Lived Proteins Reveals Exceptional Stability of Essential Cellular Structures. Cell 154, 971–982 (2013). [PubMed: 23993091]
23. Ozelius LJ et al. The early-onset torsion dystonia gene (DYT1) encodes an ATP-binding protein. Nat. Genet 17, 40–48 (1997). [PubMed: 9288096]
24. Kustedjo K, Bracey MH & Cravatt BF Torsin A and Its Torsion Dystonia-associated Mutant Forms Are Lumenal Glycoproteins That Exhibit Distinct Subcellular Localizations*. J. Biol. Chem 275, 27933–27939 (2000). [PubMed: 10871631]
25. Hewett J et al. TorsinA in PC12 cells: Localization in the endoplasmic reticulum and response to stress. J. Neurosci. Res 72, 158–168 (2003). [PubMed: 12671990]
26. Goodchild RE & Dauer WT Mislocalization to the nuclear envelope: An effect of the dystonia-causing torsinA mutation. Proc. Natl. Acad. Sci 101, 847–852 (2004). [PubMed: 14711988]
27. Naismith TV, Heuser JE, Breakefield XO & Hanson PI TorsinA in the nuclear envelope. Proc. Natl. Acad. Sci 101, 7612–7617 (2004). [PubMed: 15136718]
28. Gonzalez-Alegre P & Paulson HL Aberrant Cellular Behavior of Mutant TorsinA Implicates Nuclear Envelope Dysfunction in DYT1 Dystonia. J. Neurosci 24, 2593–2601 (2004). [PubMed: 15028751]
29. Gerace L TorsinA and torsion dystonia: Unraveling the architecture of the nuclear envelope. Proc. Natl. Acad. Sci 101, 8839–8840 (2004). [PubMed: 15187229]
30. Goodchild RE & Dauer WT The AAA+ protein torsinA interacts with a conserved domain present in LAP1 and a novel ER protein. J. Cell Biol 168, 855–862 (2005). [PubMed: 15767459]
31. Callan AC, Bunning S, Jones OT, High S & Swanton E Biosynthesis of the dystonia-associated AAA+ ATPase torsinA at the endoplasmic reticulum. Biochem. J 401, 607–612 (2006).

32. Ozelius LJ et al. Fine localization of the torsion dystonia gene (DYT1) on human chromosome 9q34: YAC map and linkage disequilibrium. Genome Res 7, 483–494 (1997). [PubMed: 9149944]
33. Ozelius LJ et al. The TOR1A (DYT1) gene family and its role in early onset torsion dystonia. Genomics 62, 377–384 (1999). [PubMed: 10644435]
34. Nery FC et al. TorsinA binds the KASH domain of nesprins and participates in linkage between nuclear envelope and cytoskeleton. J. Cell Sci 121, 3476–3486 (2008). [PubMed: 18827015]
35. Vander Heyden AB, Naismith TV, Snapp EL, Hodzic D & Hanson PI LULL1 retargets TorsinA to the nuclear envelope revealing an activity that is impaired by the DYT1 dystonia mutation. Mol. Biol. Cell 20, 2661–72 (2009). [PubMed: 19339278]
36. VanGompel MJW, Nguyen KCQ, Hall DH, Dauer WT & Rose LS A novel function for the Caenorhabditis elegans torsin OOC-5 in nucleoporin localization and nuclear import. Mol. Biol. Cell 26, 1752–1763 (2015). [PubMed: 25739455]
37. Goodchild RE, Kim CE & Dauer WT Loss of the dystonia-associated protein torsinA selectively disrupts the neuronal nuclear envelope. Neuron 48, 923–932 (2005). [PubMed: 16364897]
38. Zhao C, Brown RSH, Chase AR, Eisele MR & Schlieker C Regulation of Torsin ATPases by LAP1 and LULL1. Proc. Natl. Acad. Sci 110, E1545–E1554 (2013). [PubMed: 23569223]
39. Rose AE, Brown RSH & Schlieker C Torsins: not your typical AAA+ ATPases. Crit. Rev. Biochem. Mol. Biol 50, 532–549 (2015). [PubMed: 26592310]
40. Pappas SS et al. Forebrain deletion of the dystonia protein torsinA causes dystonic-like movements and loss of striatal cholinergic neurons. eLife 4, e08352 (2015). [PubMed: 26052670]
41. Tanabe LM, Liang CC & Dauer WT Neuronal Nuclear Membrane Budding Occurs during a Developmental Window Modulated by Torsin Paralogs. Cell Rep 16, 3322–3333 (2016). [PubMed: 27653693]
42. Laudermilch E et al. Dissecting Torsin/cofactor function at the nuclear envelope: a genetic study. Mol. Biol. Cell 27, 3964–3971 (2016). [PubMed: 27798237]
43. Kim CE, Perez A, Perkins G, Ellisman MH & Dauer WT A molecular mechanism underlying the neural-specific defect in torsinA mutant mice. Proc. Natl. Acad. Sci 107, 9861–9866 (2010). [PubMed: 20457914]
44. Jacquemyn J et al. Torsin and NEP1R1-CTDNEP1 phosphatase affect interphase nuclear pore complex insertion by lipid-dependent and lipid-independent mechanisms. EMBO J 40, e106914 (2021). [PubMed: 34313336]
45. Bressman SB et al. The DYT1 phenotype and guidelines for diagnostic testing. Neurology 54, 1746–52 (2000). [PubMed: 10802779]
46. Li J, Levin DS, Kim AJ, Pappas SS & Dauer WT TorsinA restoration in a mouse model identifies a critical therapeutic window for DYT1 dystonia. J. Clin. Invest 131, (2021).
47. Otsuka S et al. Nuclear pore assembly proceeds by an inside-out extrusion of the nuclear envelope. eLife 5, e19071 (2016). [PubMed: 27630123]
48. Otsuka S & Ellenberg J Mechanisms of nuclear pore complex assembly – two different ways of building one molecular machine. FEBS Lett 592, 475–488 (2018). [PubMed: 29119545]
49. Otsuka S et al. A quantitative map of nuclear pore assembly reveals two distinct mechanisms. Nature 613, 575–581 (2023). [PubMed: 36599981]
50. Rampello AJ et al. Torsin ATPase deficiency leads to defects in nuclear pore biogenesis and sequestration of MLF2. J. Cell Biol 219, e201910185 (2020). [PubMed: 32342107]
51. Lesuisse C & Martin LJ Long-term culture of mouse cortical neurons as a model for neuronal development, aging, and death. J. Neurobiol 51, 9–23 (2002). [PubMed: 11920724]
52. Mosalaganti S et al. In situ architecture of the algal nuclear pore complex. Nat. Commun 9, 2361 (2018). [PubMed: 29915221]
53. Lin DH & Hoelz A The Structure of the Nuclear Pore Complex (An Update). Annu. Rev. Biochem 88, 725–783 (2019). [PubMed: 30883195]
54. Los GV et al. HaloTag: A Novel Protein Labeling Technology for Cell Imaging and Protein Analysis. ACS Publications https://pubs.acs.org/doi/pdf/10.1021/cb800025k (2008) doi:10.1021/cb800025k.

55. Rabut G, Doye V & Ellenberg J Mapping the dynamic organization of the nuclear pore complex inside single living cells. Nat. Cell Biol 6, 1114–1121 (2004). [PubMed: 15502822]
56. Dultz E & Ellenberg J Live imaging of single nuclear pores reveals unique assembly kinetics and mechanism in interphase. J. Cell Biol 191, 15–22 (2010). [PubMed: 20876277]
57. Lodin Z, Blumajer J & Mares V Nuclear pore complexes in cells of the developing mouse cerebral cortex. Acta Histochem 63, 74–79 (1978). [PubMed: 105558]
58. Jokhi V et al. Torsin Mediates Primary Envelopment of Large Ribonucleoprotein Granules at the Nuclear Envelope. Cell Rep 3, 988–995 (2013). [PubMed: 23583177]
59. Liang CC, Tanabe LM, Jou S, Chi F & Dauer WT TorsinA hypofunction causes abnormal twisting movements and sensorimotor circuit neurodegeneration. J. Clin. Invest 124, 3080–3092 (2014). [PubMed: 24937429]
60. Maul GG, Price JW & Lieberman MW Formation and Distribution of Nuclear Pore Complexes in Interphase. J. Cell Biol 51, 405–418 (1971). [PubMed: 5165267]
61. Maul G & Deaven L Quantitative determination of nuclear pore complexes in cycling cells with differing DNA content. J. Cell Biol 73, 748–760 (1977). [PubMed: 406262]
62. Maul GG, Deaven LL, Freed JJ, Campbell LM & Beçak W Investigation of the determinants of nuclear pore number. Cytogenet. Genome Res 26, 175–190 (1980).
63. Maul GG et al. Time Sequence of Nuclear Pore Formation in Phytohemagglutinin-stimulated Lymphocytes and in HeLa Cells during the Cell Cycle. J. Cell Biol 55, 433–447 (1972). [PubMed: 5076782]
64. D'Angelo MA, Anderson DJ, Richard E & Hetzer MW Nuclear Pores Form de Novo from Both Sides of the Nuclear Envelope. Science 312, 440–443 (2006). [PubMed: 16627745]
65. Maeshima K et al. Nuclear pore formation but not nuclear growth is governed by cyclin-dependent kinases (Cdks) during interphase. Nat. Struct. Mol. Biol 17, 1065–1071 (2010). [PubMed: 20711190]
66. Varberg JM, Unruh JR, Bestul AJ, Khan AA & Jaspersen SL Quantitative analysis of nuclear pore complex organization in Schizosaccharomyces pombe. Life Sci. Alliance 5, (2022).
67. Doucet CM, Talamas JA & Hetzer MW Cell Cycle-Dependent Differences in Nuclear Pore Complex Assembly in Metazoa. (2010) doi:10.1016/j.cell.2010.04.036.
68. Doucet CM & Hetzer MW Nuclear pore biogenesis into an intact nuclear envelope. Chromosoma 119, 469–477 (2010). [PubMed: 20721671]
69. Maul GG The nuclear and the cytoplasmic pore complex: structure, dynamics, distribution, and evolution. Int. Rev. Cytol. Suppl 75–186 (1977). [PubMed: 348630]
70. Bucci M & Wente SR In vivo dynamics of nuclear pore complexes in yeast. J. Cell Biol 136, 1185–1199 (1997). [PubMed: 9087436]
71. Belgareh N & Doye V Dynamics of Nuclear Pore Distribution in Nucleoporin Mutant Yeast Cells. J. Cell Biol 136, 747–759 (1997). [PubMed: 9049242]
72. Romanauska A & Köhler A The Inner Nuclear Membrane Is a Metabolically Active Territory that Generates Nuclear Lipid Droplets. Cell 174, 700–715.e18 (2018). [PubMed: 29937227]
73. Ohsaki Y et al. PML isoform II plays a critical role in nuclear lipid droplet formation. J. Cell Biol 212, 29–38 (2016). [PubMed: 26728854]
74. Merta H & Bahmanyar S The Inner Nuclear Membrane Takes On Lipid Metabolism. Dev. Cell 47, 397–399 (2018). [PubMed: 30458132]
75. Sołtysik K, Ohsaki Y, Tatematsu T, Cheng J & Fujimoto T Nuclear lipid droplets derive from a lipoprotein precursor and regulate phosphatidylcholine synthesis. Nat. Commun 10, 473 (2019). [PubMed: 30692541]
76. Sołtysik K et al. Nuclear lipid droplets form in the inner nuclear membrane in a seipin-independent manner. J. Cell Biol 220, e202005026 (2021). [PubMed: 33315072]
77. Lee S, Merta H, Rodríguez JWC & Bahmanyar S A membrane sensing mechanism couples local lipid metabolism to protein degradation at the inner nuclear membrane. 2022.07.06.498903 Preprint at 10.1101/2022.07.06.498903 (2022).
78. Mathiowetz AJ et al. CLCC1 promotes hepatic neutral lipid flux and nuclear pore complex assembly. 2024.06.07.597858 Preprint at 10.1101/2024.06.07.597858 (2024).

79. Grillet M et al. Torsins Are Essential Regulators of Cellular Lipid Metabolism. Dev. Cell 38, 235–247 (2016). [PubMed: 27453503]
80. Cascalho A et al. Excess Lipin enzyme activity contributes to TOR1A recessive disease and DYT-TOR1A dystonia. Brain 143, 1746–1765 (2020). [PubMed: 32516804]
81. Shin J-Y et al. Nuclear envelope–localized torsinA-LAP1 complex regulates hepatic VLDL secretion and steatosis. J. Clin. Invest 129, 4885–4900 (2019). [PubMed: 31408437]
82. Prophet SM et al. Atypical nuclear envelope condensates linked to neurological disorders reveal nucleoporin-directed chaperone activities. Nat. Cell Biol 24, 1630–1641 (2022). [PubMed: 36302970]
83. Kuiper EFE et al. The chaperone DNAJB6 surveils FG-nucleoporins and is required for interphase nuclear pore complex biogenesis. Nat. Cell Biol 24, 1584–1594 (2022). [PubMed: 36302971]
84. Keuenhof KS et al. Nuclear envelope budding and its cellular functions. Nucleus 14, 2178184 (2023). [PubMed: 36814098]
85. Li J, Liang C-C, Pappas SS & Dauer WT TorsinB overexpression prevents abnormal twisting in DYT1 dystonia mouse models. eLife 9, e54285 (2020). [PubMed: 32202496]
86. Quartarone A & Hallett M Emerging concepts in the physiological basis of dystonia. Mov. Disord. Off. J. Mov. Disord. Soc 28, 958–967 (2013).
87. Quartarone A & Ghilardi MF Chapter 14 - Neuroplasticity in dystonia: Motor symptoms and beyond. in Handbook of Clinical Neurology (eds. Quartarone A, Ghilardi MF & Boller F) vol. 184 207–218 (Elsevier, 2022).
88. Yellajoshyula D, Opeyemi S, Dauer WT & Pappas SS Genetic evidence of aberrant striatal synaptic maturation and secretory pathway alteration in a dystonia mouse model. Dystonia 0, (2022).
89. Song C-H et al. Subtle microstructural changes of the striatum in a DYT1 knock-in mouse model of dystonia. Neurobiol. Dis 54, 362–371 (2013). [PubMed: 23336980]
90. Song C-H, Bernhard D, Hess EJ & Jinnah HA Subtle microstructural changes of the cerebellum in a knock-in mouse model of DYT1 dystonia. Neurobiol. Dis 62, 372–380 (2014). [PubMed: 24121114]
91. Vanni V et al. Cerebellar synaptogenesis is compromised in mouse models of DYT1 dystonia. Exp. Neurol 271, 457–467 (2015). [PubMed: 26183317]
92. Maltese M et al. Early structural and functional plasticity alterations in a susceptibility period of DYT1 dystonia mouse striatum. eLife 7, e33331 (2018). [PubMed: 29504938]
93. Capelson M et al. Chromatin-Bound Nuclear Pore Components Regulate Gene Expression in Higher Eukaryotes. Cell 140, 372–383 (2010). [PubMed: 20144761]
94. Ibarra A & Hetzer MW Nuclear pore proteins and the control of genome functions. Genes Dev 29, 337–349 (2015). [PubMed: 25691464]
95. Pascual-Garcia P et al. Metazoan Nuclear Pores Provide a Scaffold for Poised Genes and Mediate Induced Enhancer-Promoter Contacts. Mol. Cell 66, 63–76.e6 (2017). [PubMed: 28366641]
96. Sun J, Shi Y & Yildirim E The Nuclear Pore Complex in Cell Type-Specific Chromatin Structure and Gene Regulation. Trends Genet 35, 579–588 (2019). [PubMed: 31213386]
97. Kadota S et al. Nucleoporin 153 links nuclear pore complex to chromatin architecture by mediating CTCF and cohesin binding. Nat. Commun 11, 2606 (2020). [PubMed: 32451376]
98. Toda T et al. Nup153 Interacts with Sox2 to Enable Bimodal Gene Regulation and Maintenance of Neural Progenitor Cells. Cell Stem Cell 21, 618–634.e7 (2017). [PubMed: 28919367]
99. Orniacki C et al. Y-complex nucleoporins independently contribute to nuclear pore assembly and gene regulation in neuronal progenitors. J. Cell Sci 136, jcs261151 (2023). [PubMed: 37305998]
100. Jacinto FV, Benner C & Hetzer MW The nucleoporin Nup153 regulates embryonic stem cell pluripotency through gene silencing. Genes Dev 29, 1224–1238 (2015). [PubMed: 26080816]
101. D'Angelo MA, Gomez-Cavazos JS, Mei A, Lackner DH & Hetzer MW A Change in Nuclear Pore Complex Composition Regulates Cell Differentiation. Dev. Cell 22, 446–458 (2012). [PubMed: 22264802]

102. Lupu F, Alves A, Anderson K, Doye V & Lacy E Nuclear Pore Composition Regulates Neural Stem/Progenitor Cell Differentiation in the Mouse Embryo. Dev. Cell 14, 831–842 (2008). [PubMed: 18539113]

103. Li J, Kim S, Pappas SS & Dauer WT CNS critical periods: implications for dystonia and other neurodevelopmental disorders. JCI Insight 6, (2021).

Methods-only References

104. Grimm JB et al. A general method to improve fluorophores for live-cell and single-molecule microscopy. Nat. Methods 12, 244–250 (2015). [PubMed: 25599551]

105. Grimm JB et al. A General Method to Improve Fluorophores Using Deuterated Auxochromes. JACS Au 1, 690–696 (2021). [PubMed: 34056637]

106. Shaw TR et al. Estimating the localization spread function of static single-molecule localization microscopy images. Biophys. J 121, 2906–2920 (2022). [PubMed: 35787472]

107. Chozinski TJ et al. Expansion Microscopy with Conventional Antibodies and Fluorescent Proteins. Nat. Methods 13, 485–488 (2016). [PubMed: 27064647]

108. Asano SM et al. Expansion Microscopy: Protocols for Imaging Proteins and RNA in Cells and Tissues. Curr. Protoc. Cell Biol 80, e56 (2018). [PubMed: 30070431]

109. Gambarotto D et al. Imaging cellular ultrastructures using expansion microscopy (U-ExM). Nat. Methods 16, 71–74 (2019). [PubMed: 30559430]

110. Phan S et al. 3D reconstruction of biological structures: automated procedures for alignment and reconstruction of multiple tilt series in electron tomography. Adv. Struct. Chem. Imaging 2, 8 (2016). [PubMed: 27547706]

111. Schindelin J et al. Fiji: an open-source platform for biological-image analysis. Nat. Methods 9, 676–682 (2012). [PubMed: 22743772]

112. Veatch SL et al. Correlation Functions Quantify Super-Resolution Images and Estimate Apparent Clustering Due to Over-Counting. PLOS ONE 7, e31457 (2012). [PubMed: 22384026]

113. Ester M, Kriegel H-P, Sander J & Xu X A Density-Based Algorithm for Discovering Clusters in Large Spatial Databases with Noise.

114. Heydarian H et al. Template-free 2D particle fusion in localization microscopy. Nat. Methods 15, 781–784 (2018). [PubMed: 30224671]

115. Lord SJ, Velle KB, Mullins RD & Fritz-Laylin LK SuperPlots: Communicating reproducibility and variability in cell biology. J. Cell Biol 219, e202001064 (2020). [PubMed: 32346721]

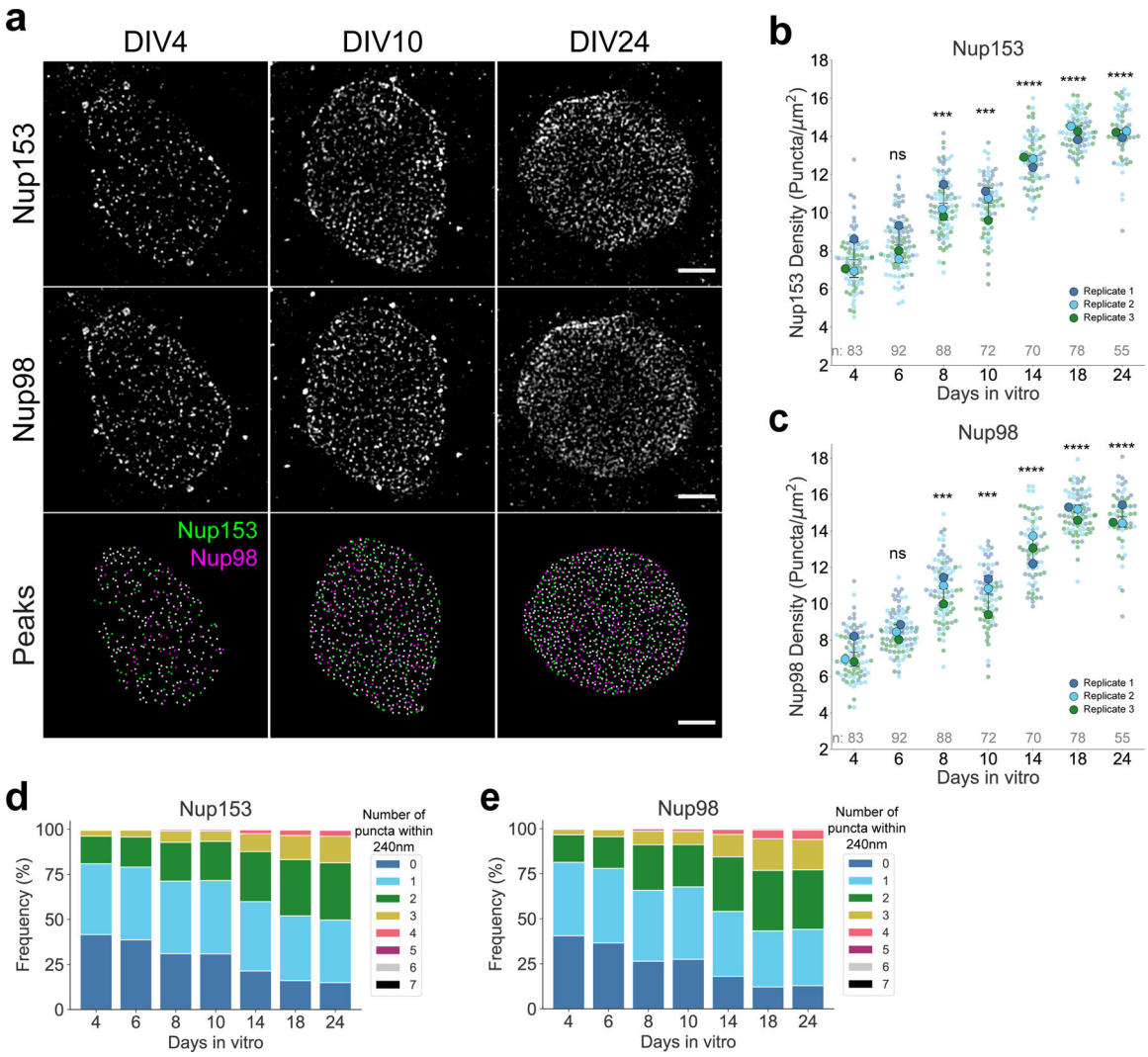

Figure 1: Nuclear pore complex biogenesis is upregulated during neuronal maturation

a, Structured illumination microscopy (SIM) images of primary neurons aged DIV4, 10, and 24 labeled with anti-Nup153 and anti-Nup98 antibodies. Bottom row shows identified Nup153 and 98 peaks. Representative images from 3 biological replicates. Scale bar = 2μm.

b, Superplots of Nup153 density (puncta/μm^2) over time in primary neurons. Plots show mean ± SD from 3 biological replicates. One-way ANOVA with Dunnett's multiple comparisons test was performed, with DIV4 as the reference condition. ***P=0.0007, ****P<0.0001. Total number of analyzed nuclei are represented as "n".

c, Superplots of Nup98 density (puncta/μm^2) over time in primary neurons. Plots show mean ± SD from 3 biological replicates. One-way ANOVA with Dunnett's multiple comparisons test was performed, with DIV4 as the reference condition. ***P=0.0001 (DIV4 vs. DIV8), ***P=0.0003 (DIV4 vs. DIV10), ****P<0.0001.

d, e, Frequency distribution of Nup153 (**d**) and Nup98 (**e**) puncta found within two-pore diameter (240nm) distance. For each identified Nup153 and Nup98 peak, the number of neighboring puncta within a radius of 240nm was calculated. Results from three biological replicates were combined at each timepoint.

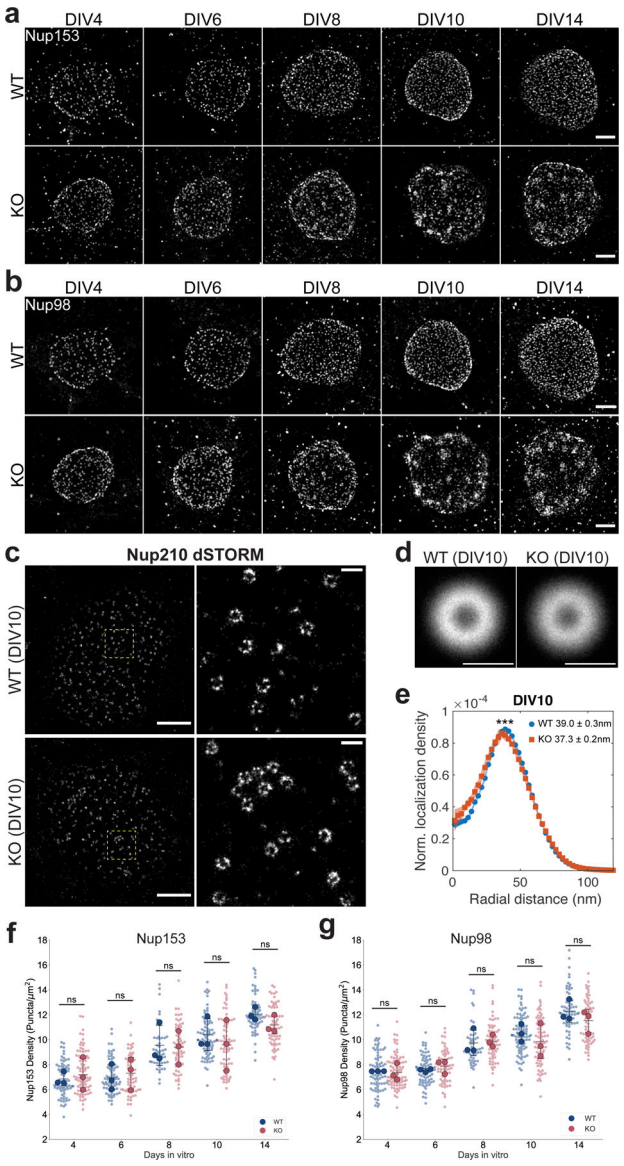

Figure 2: TorsinA is essential for uniform NPC distribution but not upregulation of NPC biogenesis

a, b, SIM images of WT and torsinA-KO primary neurons aged DIV4, 6, 8, 10, and 14 labeled with anti-Nup153 (**a**) and anti-Nup98 (**b**) antibodies. Representative images from 3 biological replicates. Scale bar = 2μm.

c, dSTORM images of Nup210-labeled NPCs in DIV10 WT and torsinA-KO neurons. Scale bar = 2μm. Right panels show zoomed in view of boxed regions. Scale bar of right panels = 200nm. 16 WT cells from 4 biological replicates and 18 torsinA-KO cells from 5 biological replicates were imaged.

d, Averaged aligned DIV10 WT and torsinA-KO pores. Scale bar = 100nm.

e, Normalized localization density along radial distance in averaged WT and torsinA-KO pores. Plots show mean ± SEM from eight bootstrapping rounds with 250 randomly selected pores each. No adjustments were made. ***P=0.0005, two-tailed t-test.

f, g, Nup153 (**f**) and Nup98 (**g**) density (puncta/μm^2) in maturing primary neurons. Plots show mean ± SD from 3 biological replicates. Timepoints from each replicate were matched and repeated measures two-way ANOVA with Sidak's multiple comparisons test was performed to compare means between genotypes. ns, not significant.

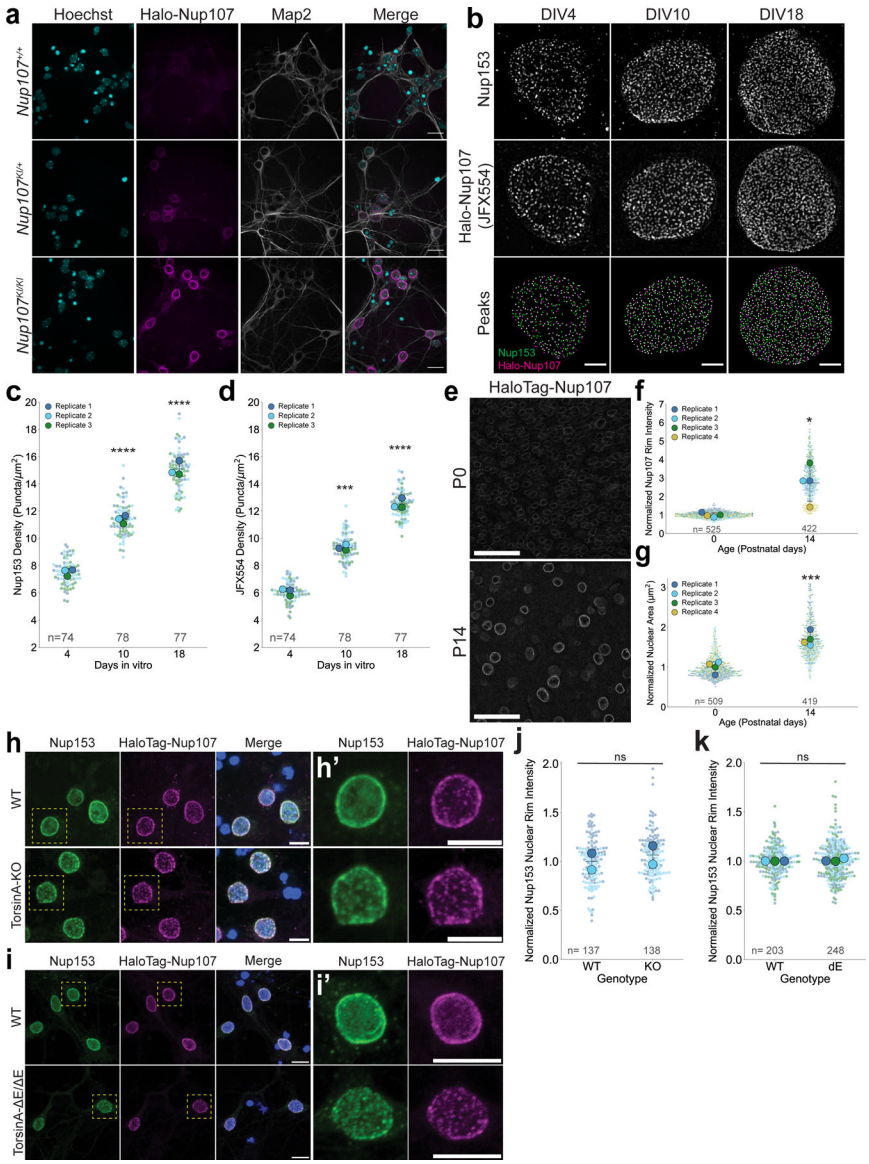

Figure 3: Neurons bearing HaloTag-Nup107 knock-in alleles demonstrate endogenous NPC upregulation

a, Confocal images of DIV10 *Nup107*$^{+/+}$, *Nup107*$^{KI/+}$, and *Nup107*$^{KI/KI}$ neurons labeled with JF646 HaloTag ligand. Scale bar = 20μm. Representative images from three biological replicates.

b, SIM images of *Nup107*$^{KI/KI}$ neurons at DIV4, 10, and 18 labeled with JFX554 HaloTag ligand and anti-Nup153 antibody.

c, d, Superplots of Nup153 (**c**) and JFX554 (**d**) puncta density in primary neurons aged DIV4, 10, 18. Plots show mean ± SD from 3 biological replicates. ***P=0.0002, ****P<0.0001; One-way ANOVA with Dunnett's multiple comparisons test, with DIV4 as the reference condition. "n", number of analyzed nuclei.

e, Confocal images of P0 and P14 cortical brain sections from *Tor1a*$^{+/+}$;*Nup107*$^{KI/KI}$ mice labeled with JFX650 HaloTag ligand. Scale bar = 50μm.

f, Normalized JFX554 HaloTag-Nup107 nuclear rim intensity from P0 and P14 cortical brain sections. All measurements were normalized to the mean intensity of P0 brain sections. Plots show mean ± SD; four biological replicates. *P=0.0379; two-tailed unpaired t-test with Welch's correction. "n", number of analyzed nuclei.

g, Normalized nuclear area based on ROIs used in (**f**). All measurements were normalized to the mean nuclear area of P0 nuclei. Plots show mean ± SD; four biological replicates. ***P=0.0009; two-tailed unpaired t-test with Welch's correction. "n", number of analyzed nuclei.

h, Confocal maximum intensity projection of DIV10 WT and torsinA-KO neurons expressing HaloTag-Nup107 labeled with JF646 HaloTag ligand and anti-Nup153 antibody. Merge shows Hoechst (blue), JF646 (magenta), and Nup153 (green). Scale bar = 10μm.

h', Zoomed-in view of cells in yellow boxes in (**h**). Scale bar = 10μm.

i, Confocal maximum intensity projection of DIV10 WT and torsinA-ΔE/ΔE neurons expressing HaloTag-Nup107 labeled with JF646 HaloTag ligand and anti-Nup153 antibody. Merge shows Hoechst (blue), JFX554 (magenta), and Nup153 (green). Scale bar = 10μm.

i', Zoomed-in view of cells in yellow boxes in (**i**). Scale bar = 10μm.

j, k, Normalized Nup153 nuclear rim intensity from DIV10 WT and torsinA-KO (**j**) and WT and torsinA-ΔE/ΔE (**k**) neurons. Intensity values were normalized to the mean of WT intensities. Plots show mean ± SD from two (**j**) or three (**k**) biological replicates. ns, not significant; two-tailed paired t-test. "n", number of analyzed nuclei.

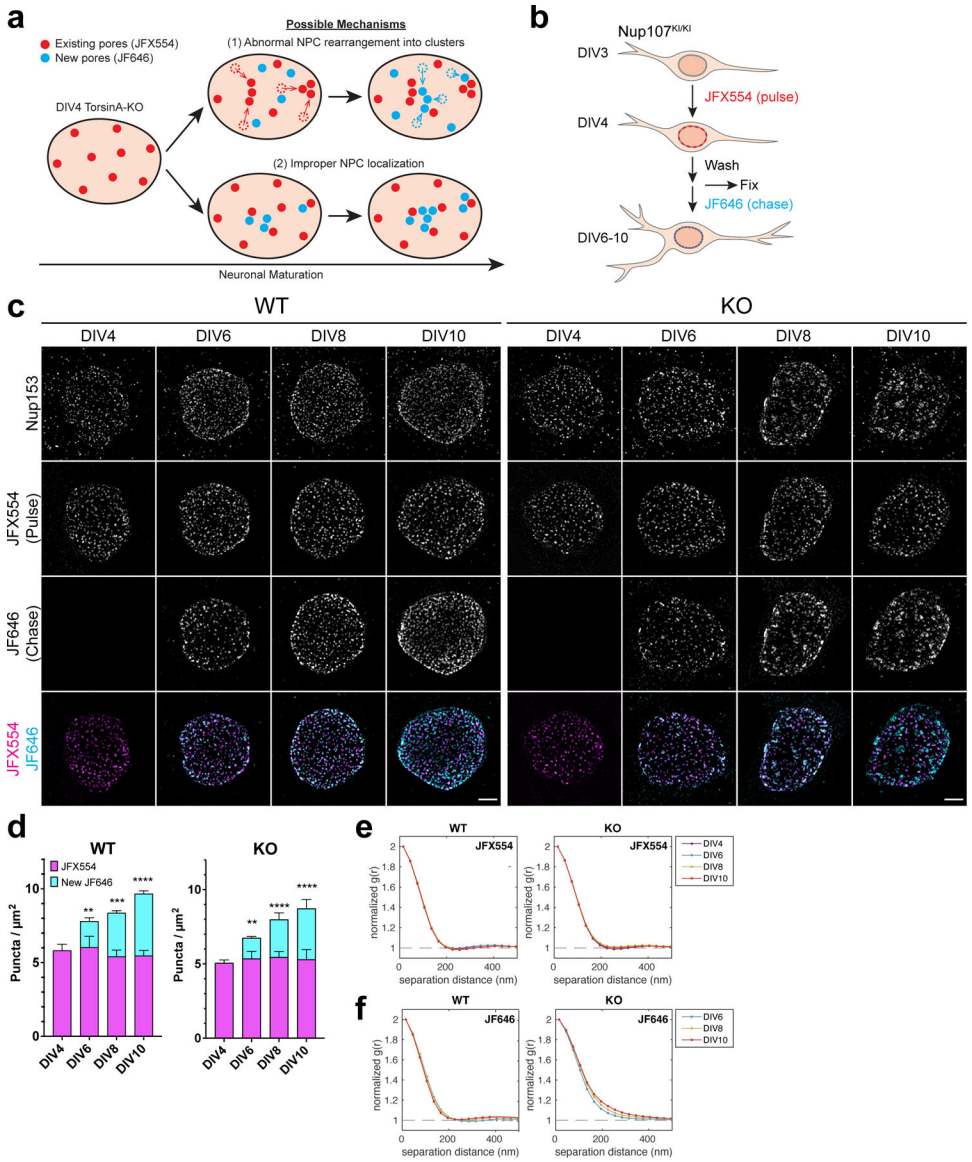

Figure 4: Sites of NPC biogenesis are abnormal in torsinA-KO neurons

a, Diagram of potential mechanisms for NPC clustering in torsinA-KO neurons. In (1), NPCs redistribute after formation, leading to clusters of existing and newly formed NPCs. In (2), sites of NPC biogenesis are mislocalized and clusters exclusively contain new NPCs. Red circles represent existing NPCs (pulse; JFX554). Blue circles represent new NPCs (chase; JF646).

b, Schematic of HaloTag pulse-chase experiment.

c, HaloTag pulse-chase SIM images of WT and torsinA-KO neurons. Neurons were stained with anti-Nup153 antibody post-fixation to label the total NPC population. Scale bar = 2µm.

d, Density of JFX554 puncta and new JF646 puncta in DIV 4, 6, 8, and 10 WT and torsinA-KO HaloTag-Nup107 neurons. Plots show mean ± SD from 3 biological replicates. Repeated measures two-way ANOVA with Dunnett's test was performed with DIV4 values as a

reference. **P=0.0024, ***P=0.003, ****P<0.0001 for WT; **P=0.0076, ****P<0.0001 for KO.

e, Normalized autocorrelation of JFX554 SIM images over 0–500nm separation distance. Autocorrelation values <1 around 200nm in both WT and torsinA-KO neurons reflect nonrandom uniform distribution of JFX554-labeled NPCs.

f, Normalized autocorrelation of JF646 SIM images over 0–500nm separation distance. Autocorrelation values >1 in torsinA-KO neurons reflect clustering of NPCs labeled with JF646.

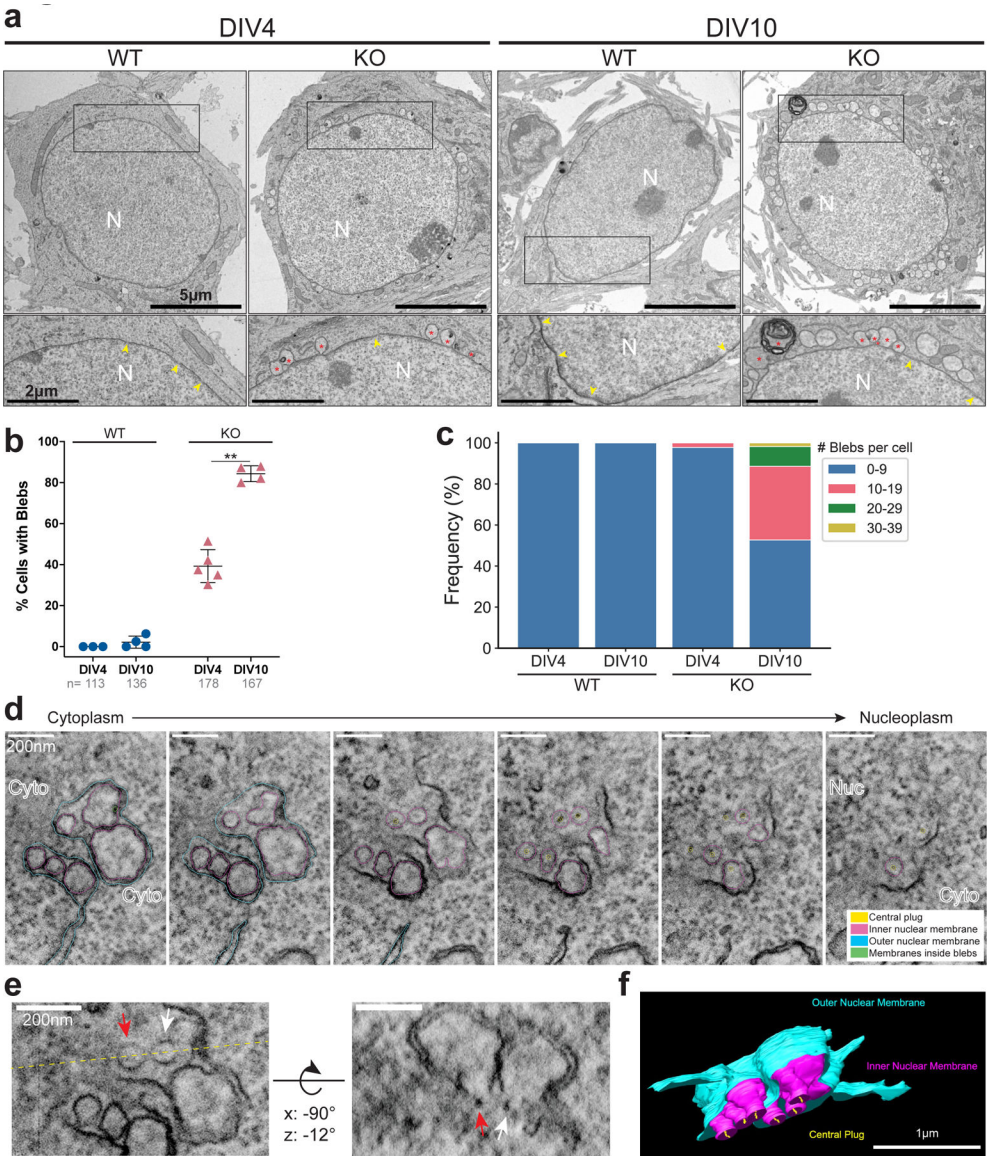

Figure 5: NE blebs spatially and temporally coincide with NPC biogenesis

a, Transmission electron microscopy (TEM) images of WT and torsinA-KO neurons at DIV4 and DIV10. N=nucleus. Fully-formed NPCs are marked with yellow arrowheads. NE blebs identified by blinded analysis are marked with red asterisks. Scale bar = 5μm for the top row, 2μm for inset. Images were acquired from at least three biological replicates for each genotype at each timepoint.

b, Quantitation of TEM images. Plots show mean ± SD. Each point represents the % of cells with at least one NE bleb from each biological replicate. **P=0.0043, two-tailed paired t-test. Total number of analyzed nuclei are represented as “n”.

c, Frequency of NE blebs per cell from all replicates.

d, Slices from a DIV10 torsinA-KO tomogram overlayed with segmented contours of the outer nuclear membrane (cyan), inner nuclear membrane (magenta), membranes inside blebs

(green), and central plug of pores (yellow). Tomogram shown here is representative of 8 tomograms from two biological replicates.

e, Rotated view of tomogram in (**d**) to show an XY view intersecting the center of two blebs at the yellow dashed line. Red and white arrows label bleb-associated pores with central plugs. The rotated view (right) demonstrates that these pores form the base of each bleb.

f, Segmented bleb clusters from a DIV10 torsinA-KO tomogram. Scale bar = 1μm. 3D view is available in Supplementary Video 2.

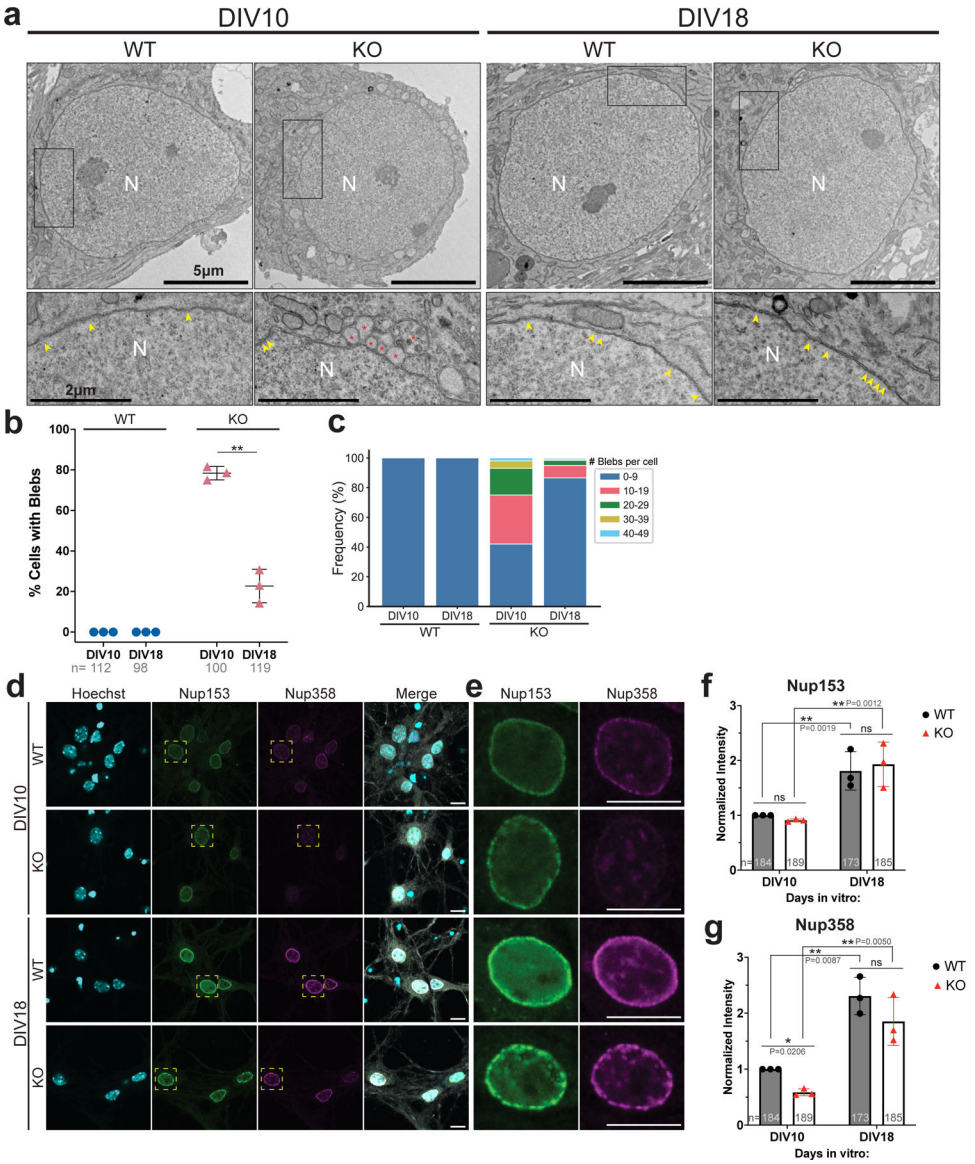

Figure 6: NPC assembly completes following NE bleb resolution

a, TEM images of WT and torsinA-KO neurons at DIV10 and DIV18. N=nucleus. Fully formed NPCs are marked with yellow arrowheads. NE blebs identified in blinded analysis are marked with red asterisks. Scale bar= 5μm for the top row, 2μm for inset. Images were acquired from three biological replicates for each genotype at each timepoint.

b, Quantitation of TEM images. Plots show mean ± SD from 3 biological replicates. Each point represents the % of cells with at least one NE bleb from each biological replicate. Total number of analyzed nuclei are represented as "n". **P=0.006; two-tailed paired t-test.

c, Frequency of NE blebs per cell from all replicates.

d, Confocal images of DIV10 and DIV18 WT and torsinA-KO neurons labeled with Hoechst, Nup153, Nup358, and Map2 (shown in merge). Scale bar = 10μm.

e, Zoomed in view of Nup153 and Nup358 channels of nuclei marked with yellow boxes in (**d**). Scale bar = 10μm.

f, g, Normalized Nup153 (**f**) and Nup358 (**g**) nuclear rim intensity of DIV10 and DIV18 WT and torsinA-KO primary neurons. Plots show mean ± SD from 3 biological replicates. ns, not significant; **P <0.01, repeated measures two-way ANOVA with Sidak's multiple comparisons test. For (**f**), **P=0.0019 for WT and **P=0.0012 for torsinA-KO DIV10 vs. DIV18; For (**g**), *P=0.0206 for DIV10 WT vs. torsinA-KO, **P=0.0087 for WT DIV10 vs. DIV18 and **P=0.0050 for torsinA-KO DIV10 vs. DIV18.